Quaternary International 757 (2026) 110101

Contents lists available at ScienceDirect

Quaternary International

journal homepage: www.elsevier.com/locate/quaint

Optical dating of Holocene extreme flood events in eastern South Africa and their connection to ENSO variability

Jamie C. Wood [a,*], Phillip S. Toms [a], Michael C. Grenfell [b], Marc S. Humphries [c]

[a] Luminescence Dating Laboratory, University of Gloucestershire, Cheltenham, UK
[b] Institute for Water Studies, Department of Earth Science, University of the Western Cape, Bellville, South Africa
[c] School of Chemistry, University of the Witwatersrand, Johannesburg, South Africa

ARTICLE INFO

Keywords:
Blocked-valley lake
Fluvial
OSL
Quartz
Tributary
Wetland

ABSTRACT

Existing research examining tributary blocked-valley lake and wetland development upon the Mfolozi River floodplain (South African east coast) has highlighted the potential for blocked-valley lakes to act as mainstem palaeoflood archives. Sand and silt units preserved within the organic deposits of these floodplain-impounded features represent relatively large flood events and provide an opportunity to establish the frequency of extreme flooding in the region beyond the timespan of instrumental and historical records, thereby helping to reduce uncertainty around future tropical cyclone activity in a warming world. However, absolute age estimates for these sequences have been limited to radiocarbon dating of organic units, restricting flood history reconstruction. This study had two inter-related aims. Firstly, to evaluate the use of optically stimulated luminescence (OSL) dating for chronicling clastic sediments associated with the floodplain's blocked-valley lakes. Secondly, in combination with radiocarbon dating and Bayesian age-depth modelling, to reconstruct flood history across three sites on the Mfolozi floodplain and investigate the climatic factors that drove past extreme flooding in the region. The Finite Mixture Model (FMM) applied to single grain OSL data was identified as the most suitable equivalent dose (D_e) model, producing age estimates that either aligned with historical records and/or accounted for the largest population of grains with a common dose. The deposition models developed provide evidence for the occurrence of multiple extreme floods since the first event identified at 7.2 ka, providing the first long-term flood record for the region. Comparison of the Mfolozi palaeoflood record with independent sedimentary hydroclimatic evidence from the region indicates a historical tendency for more frequent extreme floods during weakened El Niño conditions (i.e., La Niña or neutral ENSO phases). This suggests that variations in ENSO conditions through the mid-to-late Holocene likely played a fundamental role in triggering extreme flooding along South Africa's east coast.

1. Introduction

Recent reports indicate a global increase in the number of ecosystems, people and economic assets exposed to climate-related hazards (IPCC, 2022; Lange et al., 2020). Of these natural hazards, flood and storm events are the most common and from 2000 to 2019 accounted for 44 % (3254 events) and 28 % (2043 events) of global disasters, respectively. Collectively they caused an estimated annual average of ~15000 fatalities and financial losses of at least US$102 billion (CRED & UNDRR, 2020). Whilst ongoing mitigation and improvements in forecasting have reduced vulnerability to such events (e.g., Jongman et al., 2015), there remains a concern that total annual losses could rise through the co-impact of climatic change and hazard exposure. With extreme precipitation and flood events experiencing a phase of intensification (Dunn et al., 2020), there is great value and interest in exploring the nature and frequency of past events. This is particularly the case for lower income countries where, prior to the mid-1990s, relatively few flood events were recorded and reported to global hazard databases (Tanoue et al., 2016).

Limited historical flood data is an issue particularly relevant to eastern South Africa as instrumental climate records feature missing data and underreporting of high precipitation events (Kruger, 2006). In addition, climate modelling indicates that the region is particularly vulnerable and likely to experience increased exposure to extreme

* Corresponding author.
E-mail address: jwood1@glos.ac.uk (J.C. Wood).

https://doi.org/10.1016/j.quaint.2025.110101
Received 15 April 2025; Received in revised form 12 December 2025; Accepted 22 December 2025
Available online 6 January 2026

precipitation events under future global warming (Tim et al., 2023; McBride et al., 2022; Liu et al., 2021; Kendon et al., 2019; Zhang et al., 2018). Such events include tropical cyclones which develop in the Indian Ocean and occasionally make landfall on the South African coast – storm tracks for these systems are expected to extend more frequently to the KwaZulu-Natal coastline in a warming climate (Green et al., 2022). This is particularly concerning when considering the impacts of Tropical Cyclones Kenneth and Idai in 2019, which caused significant losses in neighbouring Mozambique (Nhundu et al., 2021; Kandawasvika et al., 2021).

The use of basins to extend existing records of extreme climatic events has been demonstrated for flood events (e.g. McGlue et al., 2012; Santisteban et al., 2019) and hurricanes (e.g., Madsen et al., 2009; McCloskey and Liu, 2012). Existing research on the Mfolozi floodplain, KwaZulu-Natal (Fig. 1), has highlighted the potential of blocked-valley lake basins to record flood events as clastic units within otherwise organic-rich sediment sequences (Grenfell et al., 2010). The preservation of flood sediments upon the Mfolozi floodplain provides the opportunity to extend regional palaeoflood records and, by comparing palaeoflood frequency with existing climate proxies, critically evaluate the concerning projections of climate modellers (e.g., Engelbrecht et al., 2013).

Blocked-valley lakes are underrepresented in wetland environmental research. They form when mainstem river floodplain development through lateral and vertical accretion outpaces tributary valley filling, resulting in tributary impoundment (Grenfell et al., 2010; Finlayson and Kenyon, 2007). Following disconnection from the mainstem and the establishment of shallow lake/wetland conditions, blocked-valley lake basins begin to accumulate organic material from water column productivity and from incomplete breakdown of the dominant emergent macrophyte vegetation, interlaminated with incursions of clastic sediment from mainstem floods (Grenfell et al., 2010), and occasionally

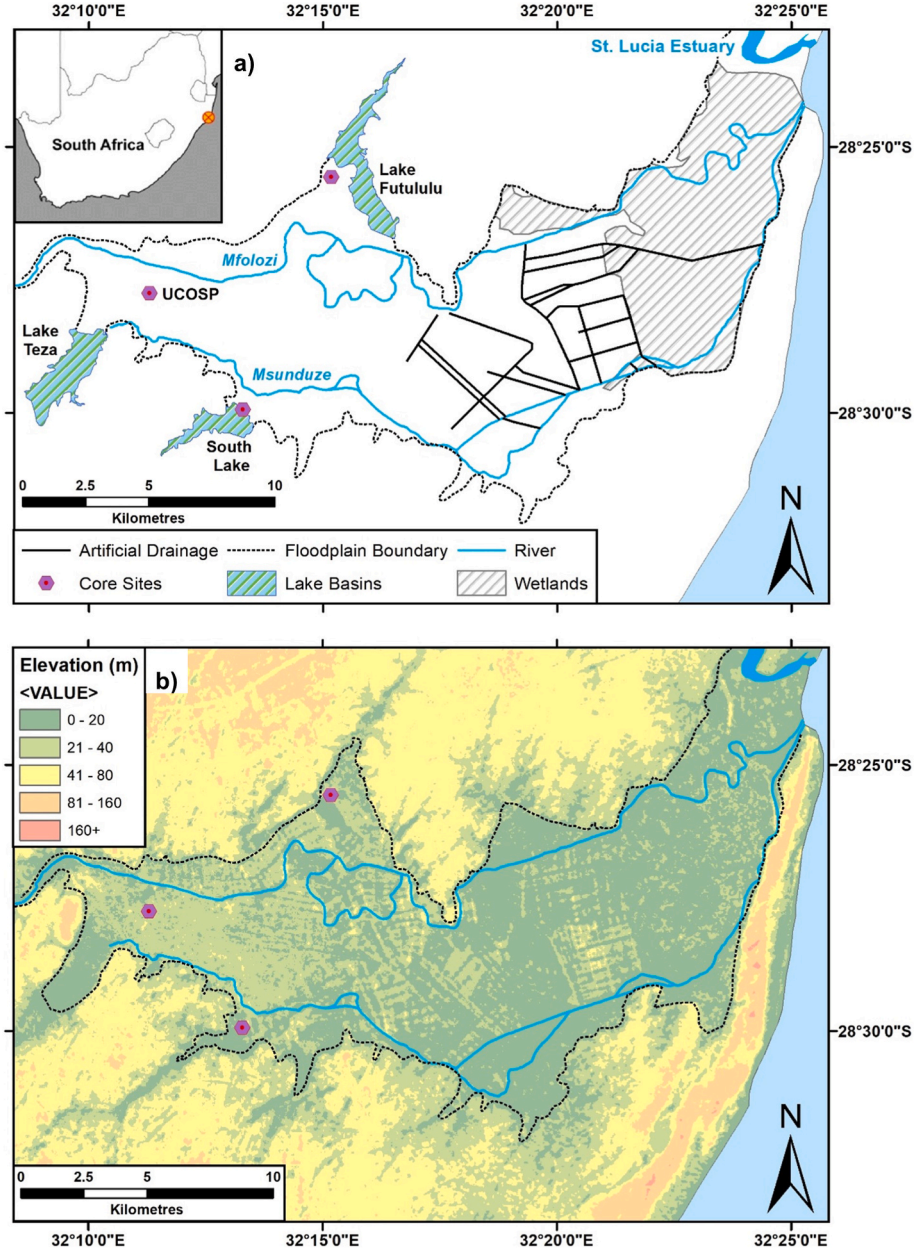

Fig. 1. a) Location of core sites on the Mfolozi floodplain (wetland extent and artificial drain locations adapted from: Grenfell et al., 2009); b) classified digital elevation model (DEM) for the Mfolozi floodplain and surrounding areas (Elevation data source: NASA/METI/AIST/Japan Space Systems and U.S./Japan ASTER Science Team, 2019).

form biologically diverse swamps (Blake and Ollier, 1971).

Blocked-valley lake basins can accumulate mainstem flood-sediment via multiple pathways (e.g., tie-channel exchange & overbank sedimentation). On the Mfolozi River floodplain overbank sedimentation is the primary mechanism. During wet seasons or periods of flooding, the mainstem river can overtop its banks and disperse sediment-laden water into tributary valleys, aided by lateral gradients across the alluvial ridge to the distal floodplain that can exceed the local longitudinal gradient. Grenfell et al. (2010) were the first to explore blocked-valley lake sedimentology in South Africa, focusing on Lake Futululu, a basin on the northern margin of the Mfolozi River floodplain (Fig. 1a). The Futululu basin supported peat formation and the preservation of interlaminated clastic lenses that fined with increasing distance from the mainstem floodplain. Grenfell et al. (2010) attributed the clastic lenses to overbank sedimentation that occurred during large floods, but were unable to directly date the clastic units, such that existing radiometric flood chronologies are limited to interpolation of a radiocarbon date-derived age-depth model.

This study evaluates optically stimulated luminescence (OSL) as a technique for dating clastic flood sediments within these blocked-valley lake deposits for the first time. Using a combination of quartz OSL dating, including sampling of several modern analogue samples, radiocarbon dating and Bayesian age-depth modelling, we present palaeoflood chronologies for three sites across the Mfolozi River floodplain. Chronologies are compared to existing proxy records from the region to interpret blocked-valley lake development and to evaluate relationships between past flood frequency and climate variability.

2. Regional setting

The Mfolozi floodplain is situated on the eastern coast of KwaZulu-Natal, South Africa (Inset – Fig. 1a). The floodplain hosts two alluvial rivers; the Mfolozi and the Msunduze, that pass eastwards over the northern and southern margins of the floodplain respectively (Fig. 1a). The Mfolozi River catchment drains an area of ~11,068 km^2 (Grenfell et al., 2009) whilst the Msunduze drains a much smaller area of ~559 km^2 (Lindsay et al., 1996). Prior to reaching the coast the two rivers meet at a confluence on the eastern margin of the floodplain and, on occasion, share an estuary with Lake St Lucia. The relatively flat floodplain is wide (Fig. 1b), spanning over 10 km across some central regions. About two thirds of the Mfolozi floodplain area is used for sugar cane cultivation and mechanically excavated drainage networks have been maintained since the 1930's for land reclamation and, more recently, for flood mitigation measures. Areas of natural wetland that remain on the floodplain are restricted to marginal lakes and the eastern-most portion of the floodplain flats (Fig. 1a). The floodplain traverses silt- and sandstone bedrock geology of the Zululand Group, which is overlain by unconsolidated aeolian deposits.

The Mfolozi floodplain is situated in the subtropical Summer Rainfall Zone (SRZ) and receives 80 % of annual precipitation (645–1090 mm) during the austral summer (Reason and Mulenga, 1999; Grenfell et al., 2009). The summer rainfall experienced by the Mfolozi catchment and SRZ, is typically associated with easterly waves and tropical systems derived from the Indian Ocean (Stager et al., 2013). Tropical-temperate troughs are recognised as the main rain-producing synoptic systems during summer over southern Africa (Manhique et al., 2011; Hart et al., 2018). These cloud bands form at the South Indian Ocean Convergence Zone (SICZ) and are sustained primarily by north-easterly moisture flux from the southwest Indian Ocean. Interannual variability in the strength and position of the SICZ, and thus cloud band development over southern Africa, is strongly linked to the El Niño-Southern Oscillation (ENSO) (Lazenby et al., 2016; Hart et al., 2018). During strong El Niño events, the SICZ shifts north-eastward, disrupting Indian Ocean moisture supply and leading to characteristically dry summer conditions and increased drought risk across southern Africa. Conversely, La Niña events are typically associated with anomalously wetter conditions and increased flood risk (Hart et al., 2018; Rapolaki et al., 2019).

Other weather systems that can also lead to substantial rainfall in the region include cut-off lows and tropical storms. Both systems have the potential to cause significant flooding and geomorphological changes across the catchment. This was demonstrated by Tropical Storm Domoina in 1984, which caused the Mfolozi to divert south into the Msunduze, with floodwaters dispersing clastic sediment that covered 90 km^2 of the Mfolozi floodplain flats (Kovacs et al., 1985; Fig. S1.1). Such events produce the flood sediments targeted for dating in this study.

3. Methods

3.1. Fieldwork

Samples were collected from three sites (Fig. 1a) across the Mfolozi floodplain in July 2014. South Lake is an infilled blocked-valley lake now dominated by palustrine wetland situated on the southern margin of the Mfolozi floodplain. Test gouge core samples from the basin highlighted the presence of both organic and clastic units within the upper 1–2 m of the basin's profile, representing a similar flood-driven sedimentology ascribed to Lake Futululu by Grenfell et al. (2010). The South Lake site was selected primarily to address the first aim of this study, to evaluate the use of OSL dating for chronicling blocked-valley lake sediments. A 4.78 m core was collected from the South Lake basin using a vibracoring system with 76 mm diameter aluminium core tubes.

The UCOSP site was an avulsion-fan sequence situated in the central region of the floodplain. The site featured an exposed section (Fig. 2) comprising sediments from four large flood events which were recorded by the Umfolozi Sugar Mill (2015 & pers.com.) in 1918, 1925, 1963 and 1984. The UCOSP site was selected for two reasons, firstly, to identify the best approach to single-grain OSL dating Mfolozi flood sediments, using the deposits of known age as modern analogues. Secondly, to provide a chronostratigraphic comparison for the blocked-valley lake palaeoflood chronology produced for South Lake. Samples from the UCOSP site were collected from the vertical section in short aluminium core tubes, and a 3.44 m vibracore sample was retrieved at the base of the section to gain additional profile depth.

The Futululu site is sited upon a crevasse splay feature, which had protruded into the Futululu blocked-valley lake basin (Fig. 1a). The crevasse splay is associated with breaches of the Mfolozi River levee following large flood events. The Futululu site was also selected to provide a chronostratigraphic comparison, enabling the consistency of

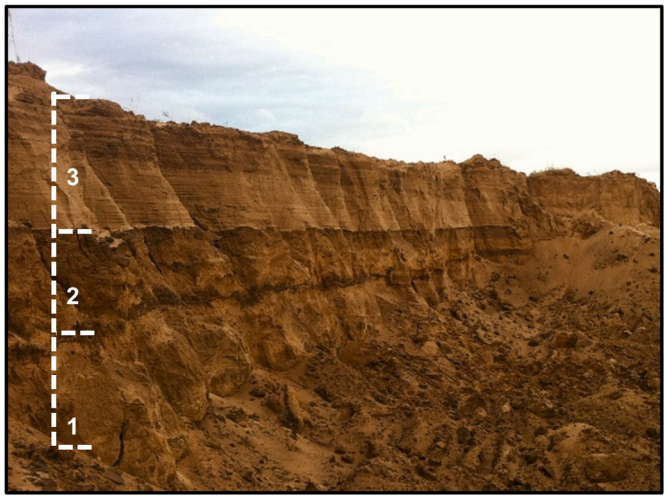

Fig. 2. Three most recent flood deposits (1925 - unit 1 – GL14004, 1963 – unit 2 – GL14003 and 1984 – unit 3 – GL14001) recorded by the UCOSP section. Depth of section: 2.2 m.

OSL dating across the floodplain to be evaluated. Samples for OSL analysis were collected at Futululu using a Cobra corer and 48 mm diameter plastic sleeves.

3.2. Core composition

Core lengths were opened and sampled under subdued red lighting conditions provided by Encapsulite RB-10 filters. Initially, small samples (*c.* 1.25 cm^3) were collected at 1 cm intervals and transferred to normal lighting conditions for loss-on-ignition (LOI_{430}; Wood, 2015) and sediment logging.

Density assessment was subsequently conducted throughout the South Lake core to assist with gamma dose modelling. The dry density of core samples was assessed at 5 cm intervals using a 5 ml syringe and 2–3 g of core material. Dry core material was compacted into a syringe and the density calculated using sample mass and compacted volume. The saturated density of the material was then calculated using a similar procedure to Nelson and Rittenour (2015). Dry samples were transferred to 15 ml centrifuge tubes and distilled water added to fill pore spaces. To achieve packing of the sediment, samples were centrifuged at 1600 RPM for 10 min. Excess water was drained after centrifuging and the saturated density calculated using packed sample mass and volume. Dry and saturated assessments were completed three times at each 5 cm interval of the South Lake core.

3.3. Equivalent dose: Preparation and measurement

Equivalent dose (D_e) samples were collected from clastic units identified by LOI_{430} and sediment logging. Samples were oven dried (40 °C) then treated with HCl (10 %) and H_2O_2 (15 %) to remove carbonates and organics, respectively. Samples were dry sieved and, for those with sufficient fine sand, sodium polytungstate density separations were conducted at 2.62 and 2.68 g/cm^3 to isolate quartz density minerals. These were treated with HF (40 %) for 60 min to remove any remaining feldspars and the alpha-irradiated (α) rind of quartz grains. The remaining material was rinsed with HCl to remove acid soluble fluorides, dried and re-sieved. 8 mm diameter quartz aliquots were prepared on aluminium discs for preheat determination (using dose recovery experiments) and multi-grain D_e assessment. For single-grain D_e acquisition, quartz within the 125–180 and 180–250 μm grain size fractions was measured upon aluminium discs comprising a 10 x 10 matrix of 200 and 300 μm holes, respectively. Further dose recovery tests using known laboratory doses were conducted on four South Lake samples at the single-grain level to assess intrinsic D_e overdispersion (OD). OD can be defined as the observed variability of a D_e distribution which is outside of that expected for a Gaussian distribution.

Fine silt quartz (5–15 μm) was isolated for samples with insufficient quantities of fine sand. Following the removal of carbonates and organics, using Stokes Law, acetone sedimentation was conducted to isolate 5–15 μm quartz and other minerals of varying size and density. The isolated material was submersed in H_2SiF_6 (35 %) for 2 weeks to remove feldspars and subsequently rinsed in HCl to remove acid soluble fluorides. A further acetone sedimentation was conducted to remove any partially digested silica (<5 μm). Approximately 1.5 mg of fine silt quartz was mounted on 9.8 mm diameter aluminium discs for D_e evaluation.

D_e measurements were conducted on a Risø TL-DA-15 TL/OSL reader (Bøtter-Jensen et al., 2000) with an updated DA-20 controller. Multi-grain stimulation was provided by blue diodes delivering a peak wavelength of 470 nm, whilst infrared (IR) diodes provided a peak wavelength of 875 nm for detecting feldspar contamination. Single-grain stimulation was delivered by a 532 nm solid state green laser focused to illuminate a 20 μm surface of each grain position (Duller et al., 1999a,b). Photon emissions were detected using an EMI 9235QA photomultiplier tube fronted with 7.5 mm of Hoya U-340 filters. Aliquot irradiation was conducted using a $^{90}Sr/^{90}Y$ beta (β) source, calibrated using sensitised quartz irradiated against the 'Hotspot 800' ^{60}Co γ source at the National Physical Laboratory, UK, delivering 0.06 Gy/s during the interval of measurement. Machine reproducibility was assessed for both single-grain (2.7 %) and multi-grain (0.7 %) aliquots (Wood, 2020).

All D_e values were quantified using the single-aliquot regenerative-dose (SAR) protocol (Murray and Wintle, 2000; Murray and Wintle, 2003; Table S2.1). For single-grain analysis, five rejection criteria were adopted to filter the grains that produced little/no signal and performed poorly during measurement. Grains were rejected if their; post-IR/OSL depletion ratio fell outside of 10 % (i.e., 1.00 ± 0.10), signal recuperation was >5 %, test signal was <3σ above background levels and recycling ratios fell outside of 10 % of unity. Errors associated with recuperation, post-IR/OSL and recycling ratios were considered when applying rejection criteria. Finally, the remaining grains were then screened to ensure D_e values did not exceed saturation limits ($2D_0$; Wintle and Murray, 2006). The initial 0.05 and 0.25 s were used for signal integration for single- and multi-grain measurements respectively. Background measurement noise was subtracted using the final 0.2 s of stimulation for single-grains and 10 s for multi-grain aliquots.

Three D_e models - the central age model (CAM - Galbraith et al., 1999), the three-parameter minimum age model (MAM-3 - Galbraith et al., 1999) and the finite mixture model (FMM - Galbraith and Green, 1990) - were applied to datasets using the 'Luminescence' package in R (Kreutzer et al., 2018). Modelled D_e values were calculated in seconds (s) of dose and then converted to Gray (Gy). Where grains with D_e values less than or statistically indistinguishable from zero were present, the un-logged MAM (MAM_{UL}; Arnold et al., 2009) D_e was also calculated. Sigma-b (σ_b) was set to 15 % for the MAM and the FMM (see section 4.2 for basis). Each application of the FMM examined models featuring between 2 and 8 components (*k*), the optimum fitting was identified by the *k* value that generated the lowest BIC (Bayes Information Criterion - Galbraith, 2005; Galbraith and Roberts, 2012). Herein, the dose component identifying the lowest D_e population (i.e. the finite mixture model minimum) is referred to as FMM_{min}, whilst the dose component with the largest grain population (i.e. the finite mixture model majority) is FMM_{maj}.

3.4. Environmental dose rate: Preparation and measurement

High-resolution gamma spectrometry (HRGS) was used to quantify the concentration of Potassium (K), Thorium (Th) and Uranium (U) (Murray and Aitken, 1988; Wood, 2020) and to assess the presence of any significant U-disequilibrium (Olley et al., 1996). Samples were oven-dried and homogenised into a fine powder using a TEMA disc mill. Between 30 and 50 g of homogenised material was sealed in 150 cc Azlon polystyrene pots with polyethylene lids and stored for at least three weeks prior to measurement for radon retention. Concentrations of K (%), Th (ppm) and U (ppm) were converted to α, β and γ dose rate (D_r) using conversion factors and associated errors provided by Liritzis et al. (2013). β attenuation, as forced by grain size, was calculated using factors determined by Mejdahl (1979) and corrected for HF etching (Brennan, 2003). Moisture attenuation was calculated using present day moisture content and factors provided by Zimmerman (1971). For fine silt quartz, an α-efficiency value (a-value) of 0.038 ± 0.002 (Rees-Jones, 1995) was adopted to account for the elevated ionising potential of α particles. The cosmogenic contribution to D_r was calculated following the steps outlined by Prescott and Hutton (1994), with an additional 10–15 % error added in quadrature to account for core compaction.

The complex sedimentology of the South Lake core required careful consideration for D_r calculation. HRGS was conducted at 5 cm intervals either side of D_e sampling locations to detect significant changes in radionuclide concentrations. Where required, D_γ modelling was conducted using the fractional dose table provided by Aitken (1985 – Appendix H) and the mean sediment density (Wood, 2020). Mean sediment density was calculated using three saturated and three dry density values for each sampling location (Fig. S3.1). The sedimentology and

dosimetry at UCOSP and Futululu displayed less variability; D_r values for these sites were calculated using radionuclide concentrations estimated for D_e sampling locations.

3.5. Independent age controls

The blocked-valley lake environment provides challenging aspects for OSL dating, particularly given the complex sedimentology, relatively low D_e values (those <20 Gy; Murray and Olley, 2002) and waterlain origin of sediments. All sediments collected from South Lake and Futululu are of unknown age making it difficult to assess the accuracy of age estimates and the utility of OSL flood chronologies. However, four different flood/avulsion deposits at the UCOSP site (Fig. 2), associated with known-age storm events that occurred over the past century (AD: 1918, 1925, 1963 and 1984), provided the opportunity to test the accuracy and precision of OSL on flood sediments from the Mfolozi.

In addition, four samples of plant material from peat units within the South Lake core were submitted to Beta Analytic for radiocarbon dating, covering depths undatable by OSL and thereby contribute to Bayesian modelling. For each sample, 5 g of organic sediment was wrapped in tin foil and placed in zip-lock bags for shipping, with Beta Analytic isolating plant macrofossils for dating. All radiocarbon samples were calibrated using the SHCal20 calibration curve (Hogg et al., 2020, Table 1). Radiocarbon and OSL dates were coupled using Bayesian age-depth modelling in OxCal v.4.2 (Bronk Ramsey, 2009), providing refined chronologies for sedimentation at each of the sites.

4. Results

4.1. Composition of Mfolozi sediments

4.1.1. UCOSP

The UCOSP core collected from below the known-age deposits was organic-poor and formed almost entirely from clastic units (Fig. 3b). The stratigraphy of the profile displayed a similar pattern to that observed in the exposed section at the site (Fig. 2); that is the alternation of fine/medium sands (lighter in colour) to silt and clay beds that harbour a little organic matter (darker colour). There are five distinct sand beds interspersed by the finer material in the basal profile (Fig. 3b).

4.1.2. Futululu

The Futululu sediment profile was also organic-poor and comprised predominantly of fine silts and clays. These beds contained some organics, but the overall content rarely exceeded 10 % below the upper 0.5 m of the core (Fig. 3c). Five fine/medium sand units were preserved within the profile. The most recent of these deposits (~0.60 m) contained material that was noticeably coarser than the sand units preserved at greater depths.

4.1.3. South Lake

The South Lake profile displayed a relatively complex sedimentology (Fig. 3a) and for ease of discussion is split into four units. The lowermost unit (1) was a clastic rich sequence, which alternated between fine/medium sand and clay rich beds. Fine/medium sand beds occupied most of unit 1.

Unit 2 and unit 3 were both characterised by distinct fluctuations in organic content (Fig. 3a – e.g. 1.14 m), created by clastic lenses preserved within organic units. The clastic lenses were composed primarily of silts and clays, but some fine/medium sands were also incorporated within their matrix. A bed formed solely of fine/medium sands was preserved at 2.10 m.

With the exception of the surface 0.1 m, the uppermost unit (4) of the site is characterised predominantly by silts and clays and was organic-poor throughout (Fig. 3a). On occasion the matrix supported fine sands, however, at these locations silts and clays remained the dominant material. One distinct change in sedimentology was notable at 0.4–0.5 m depth, where a fine/medium sand bed was preserved.

4.2. Luminescence characteristics

Multi-grain test aliquots of the Mfolozi quartz isolates displayed rapid OSL decay (Fig. 4a) and signals appeared to be dominated by the fast component. Application of the fast ratio confirmed the dominance of the fast component; for the example, the fast ratio of GL15023 (Fig. 4a) was 41.98 ± 0.87, similar to that of the calibration quartz examined by Durcan and Duller (2011). Multi-grain dose recovery tests (Fig. 4b) were used to determine preheat temperatures for all SAR D_e measurements, where the thermal treatment associated with recovered dose ratios closest to unity were selected for analysis. Samples from UCOSP and Futululu displayed similar characteristics with preheats of either 240 or 260 °C for 10 s and a cut heat of 220 °C adopted for all samples (Table 2). Most samples from the South Lake site shared these characteristics, however, there were a few exceptions, most notably for fine silt aliquots, where alternative pre-/cut heat conditions were adopted (Table 3).

Single-grain dose recovery tests were conducted on four South Lake samples to assess the intrinsic variability within D_e measurements. Values of D_e OD for the tests ranged from 7.6 to 10.1 % (Table S4.1; Fig. 4c). Whilst this provides a sense of the expected OD for a well-bleached sample and can be used as guide for the σ_b parameter in D_e modelling (see section 4.3), it is worth noting that variability in laboratory-observed OD is likely driven by a complex function of several luminescence characteristics. It is also dependent on dose and form of radiation (Thomsen et al., 2012). Furthermore, D_β heterogeneity in naturally dosed samples can further influence the intrinsic OD of a well-bleached sample (Mayya et al., 2006). Given the limited number of single-grain dose recovery tests, the uncertainty surrounding intrinsic OD and to account for scatter induced by post-burial processes, a σ_b value of 15 % was adopted for all D_e modelling.

4.3. Luminescence ages

The applicability of the three D_e models - CAM, MAM and FMM - was evaluated against the known age deposits at the UCOSP site. Galbraith and Roberts (2012) provide a comprehensive review of these models, but a brief explanation is provided here for context. OSL dating relies on minerals being exposed to sufficient sunlight prior to deposition to reset the time-dependent OSL signal. The CAM (Galbraith et al., 1999) is suitable for D_e calculation when there is minimal OD (<30 %; Arnold and Roberts, 2009), and where sediments were fully-bleached prior to burial, had similar radiation doses and experienced no post-depositional reworking (Galbraith and Roberts, 2012). The CAM assumes that log-transformed D_e (log-D_e) values are drawn from a log-normal distribution and calculates a weighted mean (δ) with a standard deviation (σ) that reflects OD.

Table 1
Radiocarbon dates (1σ confidence) for South Lake plant material.

Sample	Beta Number	Depth (m)	Radiocarbon Age (BP-1950)	$\delta^{13}C$ (‰)	1σ Calibrated Age (BC/AD)	Age (ka)
SL_AMS_1	446039	1.20	1240 ± 30	−24.8	776 - 886 AD	1.19 ± 0.06
SL_AMS_2	469558	0.90	1350 ± 30	−23.4	671 - 772 AD	1.29 ± 0.05
SL_AMS_3A	485916	1.72	1480 ± 30	−28.1	598 - 645 AD	1.39 ± 0.02
SL_AMS_5	526302	2.71	4150 ± 30	−22.1	2851 - 2583 BC	4.73 ± 0.13

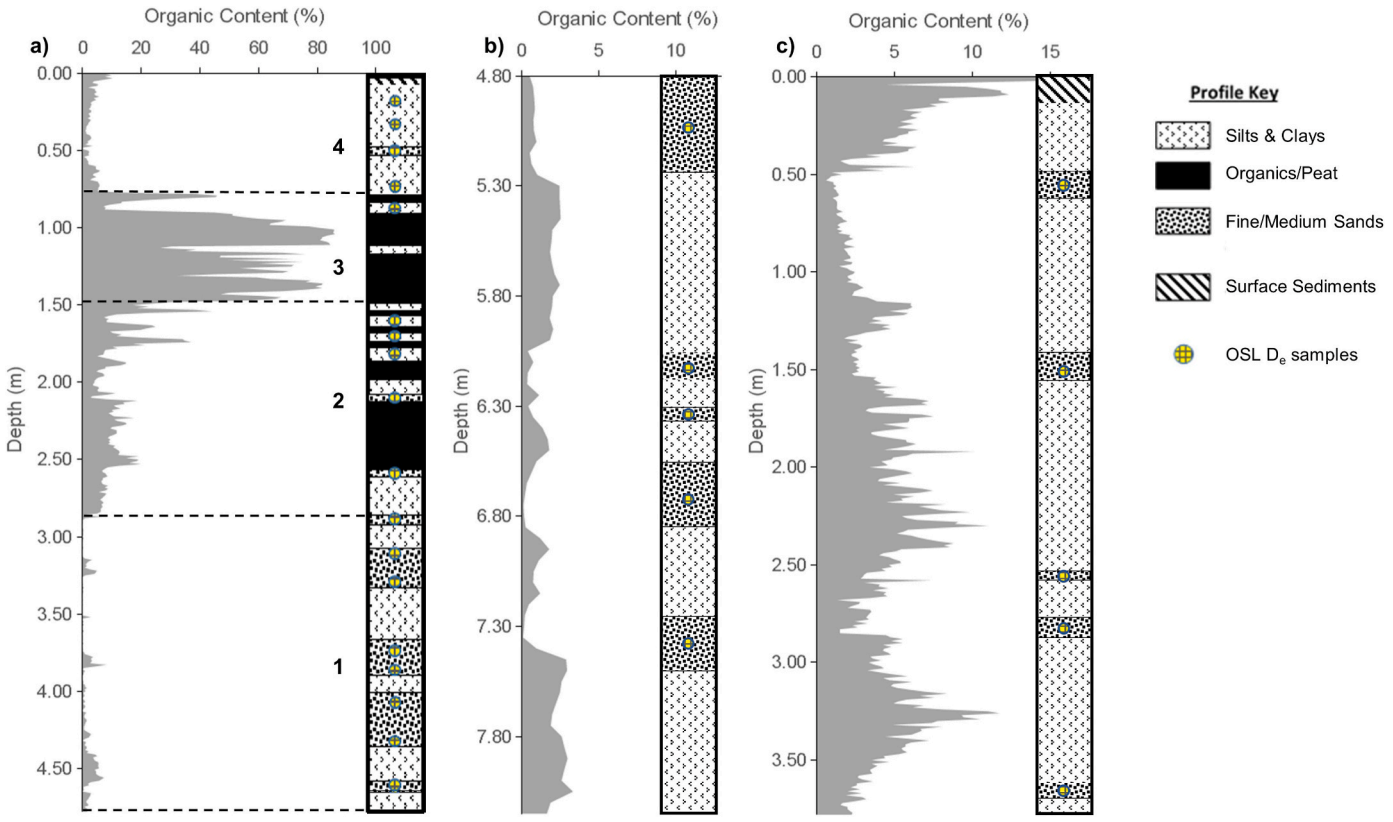

Fig. 3. LOI_{430} organic contents and sediment profiles for: a) South Lake, b) UCOSP (basal core) and c) Futululu.

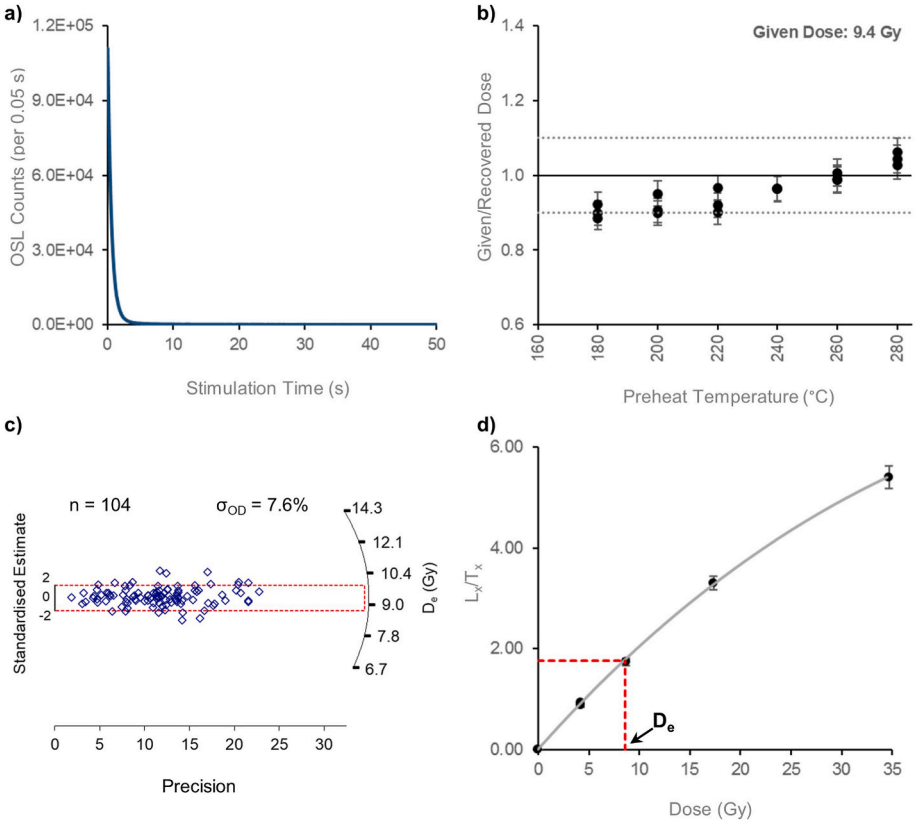

Fig. 4. Example characteristics for sample GL15023; a) OSL decay of a multi-grain test aliquot of 180–250 μm quartz, b) multi-grain dose recovery test (3 aliquots per preheat), c) radial plot for a single-grain dose recovery test (given dose: 9.4 Gy) and d) single-grain dose-response curve with regenerative doses; 0, 4.2, 8.7, 17.3 & 34.7 Gy. Interpolation of the natural L_x/T_x recovered a D_e of 8.55 Gy.

Table 2
D_e and age data for UCOSP and Futululu (MAM tested on known age UCOSP samples – FMM adopted following findings. See Tables S5.1 and S6.1 for breakdown of the FMM components).

Sample	Depth (m)	Single- (SG) or Multi-grain (MG)	Pre/Cut Heat Temp. (°C)	Grains/ Aliquots Analysed	*n*	σ_{OD} (%)	Skewness (*c*)	Kurtosis (*k*)	D_e Values (Gy)				Selected D_e Model	Age (ka)	Known Age (ka)
									CAM	MAM	FMM_{min}	FMM_{maj}			
UCOSP Section															
GL14001	0.69	SG	260/220	1500	94	>100	4.02	22.91	0.29 ± 0.03	0.07 ± 0.01	0.15 ± 0.01	0.15 ± 0.01	MAM	0.03 ± 0.01	0.03
GL14003	1.55	SG	260/220	1500	124	84	5.86	40.35	0.27 ± 0.02	0.10 ± 0.01	0.14 ± 0.01	0.26 ± 0.01	FMM_{min}	0.05 ± 0.01	0.05
GL14004	1.95	SG	260/220	1500	62	68	2.55	10.39	0.27 ± 0.03	0.19 ± 0.01	0.20 ± 0.01	0.20 ± 0.01	FMM_{min}	0.08 ± 0.01	0.09
GL14006	3.00	SG	260/220	1500	139	74	2.78	14.31	0.57 ± 0.04	0.22 ± 0.02	0.25 ± 0.01	0.42 ± 0.01	FMM_{min}	0.10 ± 0.01	0.10
UCOSP Basal Units															
GL15116	5.15	SG	240/220	1500	112	47	2.11	16.77	0.47 ± 0.02	–	0.38 ± 0.01	0.38 ± 0.01	FMM_{min}	0.18 ± 0.03	–
GL15117	6.15	SG	260/220	1500	109	23	2.97	17.37	1.40 ± 0.04	–	1.33 ± 0.03	1.33 ± 0.03	CAM	0.81 ± 0.12	–
GL15118	6.35	SG	260/220	1500	106	46	2.31	8.72	2.06 ± 0.10	–	1.32 ± 0.08	2.02 ± 0.10	FMM_{maj}	1.09 ± 0.17	–
GL15119	6.75	SG	260/220	1500	104	60	2.10	7.47	2.66 ± 0.16	–	1.58 ± 0.10	1.58 ± 0.10	FMM_{maj}	1.04 ± 0.17	–
GL15120	7.35	SG	240/220	1500	112	49	1.88	6.27	4.04 ± 0.19	–	2.54 ± 0.08	2.54 ± 0.08	FMM_{maj}	1.58 ± 0.24	–
Futululu															
GL15122	0.75	SG	240/220	1000	80	17	0.47	3.41	0.51 ± 0.01	–	0.41 ± 0.12	0.52 ± 0.03	CAM	0.21 ± 0.03	–
GL15123	1.67	SG	260/220	1000	77	39	2.09	7.79	0.54 ± 0.03	–	0.51 ± 0.01	0.51 ± 0.01	CAM	0.22 ± 0.03	–
GL15124	2.77	MG	240/220	12	12	23	–	–	4.38 ± 0.30	–	–	–	CAM	1.89 ± 0.30	–
GL15125	2.90	MG	240/220	48	48	21	–	–	4.98 ± 0.15	–	–	–	CAM	2.08 ± 0.30	–
GL15126	3.82	MG	260/220	48	48	18	–	–	4.98 ± 0.13	–	–	–	CAM	2.10 ± 0.31	–

Table 3
D_e and age data for South Lake (see Table S7.1 for breakdown of the FMM components).

Sample	Depth (m)	Grain Fraction (μm)	Single- (SG) or Multi-grain (MG)	Preheat/Cut Heat Temp. (°C)	n*	σ_{OD} (%)	Skewness (*c*)	D_e Values (Gy)			Total D_r (Gy/ ka)	Selected D_e Model	Age (ka)
								CAM	FMM_{min}	FMM_{maj}			
GL15157	0.17	180–250	SG	280/220	87	85	1.49	0.30 ± 0.03	0.11 ± 0.01	0.59 ± 0.02	2.10 ± 0.28	FMM_{min}	0.05 ± 0.01
GL15158	0.32	180–250	SG	260/220	106	77	1.15	0.32 ± 0.02	0.12 ± 0.01	0.56 ± 0.01	2.22 ± 0.30	FMM_{min}	0.05 ± 0.01
GL15015	0.48	180–250	SG	260/220	115	86	3.16	0.44 ± 0.02	0.10 ± 0.01	0.62 ± 0.01	2.33 ± 0.34	FMM_{maj}	0.27 ± 0.04
GL16099	0.72	5–15	MG	220/180	12	–	–	4.13 ± 0.05	–	–	2.67 ± 0.33	CAM	1.54 ± 0.19
GL15016	0.85	5–15	MG	220/180	12	–	–	6.09 ± 0.07	–	–	2.17 ± 0.28	CAM	2.81 ± 0.36
GL15020	1.58	5–15	MG	240/220	12	–	–	8.52 ± 0.10	–	–	2.32 ± 0.29	CAM	3.67 ± 0.47
GL15021	1.68	5–15	MG	240/220	12	–	–	7.57 ± 0.09	–	–	2.18 ± 0.27	CAM	3.47 ± 0.43
GL15022	1.81	5–15	MG	180/180	12	–	–	3.02 ± 0.03	–	–	1.64 ± 0.20	CAM	1.85 ± 0.23
GL15023	2.09	180–250	SG	260/220	140	42	0.91	10.65 ± 0.40	4.61 ± 0.19	12.50 ± 0.24	2.06 ± 0.28	$FMM_{k=2} = 7.80 \pm 0.52$	3.78 ± 0.57
GL15024	2.58	180–250	SG	240/220	136	22	3.50	6.20 ± 0.13	5.22 ± 0.42	7.07 ± 0.43	1.76 ± 0.24	CAM	3.53 ± 0.48
GL15025	2.88	180–250	SG	240/220	127	23	0.28	9.40 ± 0.22	5.99 ± 0.92	9.91 ± 0.30	1.79 ± 0.25	CAM	5.24 ± 0.73
GL15026	3.13	180–250	SG	240/220	152	21	0.44	11.92 ± 0.24	–	–	2.05 ± 0.29	CAM	5.82 ± 0.83
GL15027	3.27	180–250	SG	240/220	148	23	1.02	11.05 ± 0.24	9.45 ± 0.62	9.45 ± 0.62	1.91 ± 0.27	CAM	5.77 ± 0.81
GL15028	3.74	180–250	SG	240/220	170	24	0.81	11.21 ± 0.23	9.63 ± 0.78	12.34 ± 0.52	1.95 ± 0.27	CAM	5.74 ± 0.81
GL15029	3.87	180–250	SG	240/220	143	24	0.97	12.60 ± 0.29	11.26 ± 0.44	11.26 ± 0.44	1.97 ± 0.28	CAM	6.39 ± 0.91
GL15030	4.10	125–180	SG	240/220	187	21	0.84	14.14 ± 0.25	10.84 ± 0.73	15.37 ± 0.41	1.98 ± 0.28	CAM	7.15 ± 1.02
GL15031	4.33	125–180	SG	240/220	129	21	0.95	14.44 ± 0.30	11.91 ± 1.00	15.92 ± 0.88	2.02 ± 0.29	CAM	7.15 ± 1.02
GL15032	4.62	125–180	SG	240/220	184	22	0.50	13.04 ± 0.23	10.79 ± 0.48	14.86 ± 0.51	1.98 ± 0.28	CAM	6.59 ± 0.94

* 1000 grains analysed for each single-grain sample.

For waterlain samples that include grains that were well and incompletely bleached on deposition, the MAM (Galbraith et al., 1999) can be useful. The model assumes log-D_e values are drawn from a truncated normal distribution and considers the minimum log-D_e (γ), proportion of fully-bleached grains (ρ), plus the mean (μ) and standard deviation (σ) of the log-D_e distribution if it were non-truncated. The MAM can be fitted as a 3- (MAM-3) or 4-parameter (MAM-4) model; for the 3-parameter model γ is equal to μ. The MAM-3 was adopted in this study as it is commonly applied to partially bleached samples (Cunningham and Wallinga, 2012), numerically stable (Peng, 2021) and generally considered more robust relative to MAM-4 (Arnold et al., 2009). For D_e distributions that feature negative and zero dose values, an unlogged version of the model can be applied (MAM-3_{UL}; Arnold et al., 2009).

The FMM (Galbraith and Green, 1990) is designed to identify discrete components within a population and can be useful where multiple factors contribute to an overdispersed D_e distribution (e.g. D_β variations and incomplete bleaching; Galbraith and Roberts, 2012). The model considers a log distribution that contains normally distributed components (k) with a common standard deviation (σ). The model identifies the mean values (μ_1, μ_2, …μ_k) for each component and the proportion of D_e values encapsulated within each component (π_1, π_2, …π_k).

4.3.1. UCOSP modern analogues

The dose rates calculated for each of the known age samples were statistically consistent (i.e. overlapping uncertainties), with values ranging from 2.31 to 2.76 Gy/ka (Table 4). An elevated D_r was observed for GL14003 which appears to have been driven by a higher concentration of Th and U within the strata. There is no evidence of U-series disequilibria within the most recent flood units, with most $^{226}Ra/^{238}U$ ratios consistent with unity (Table 4). Only GL14001 is not statistically consistent with unity, however, the $^{226}Ra/^{238}U$ ratio (0.86 ± 0.11) falls well within the acceptable bounds (50 %; Olley et al., 1996) for assuming U-series equilibrium.

D_e distributions for each known-age deposit exhibit positively skewed and significantly (>30 %) overdispersed data (Table 2; Fig. S5.1), indicating the influence of factors other than counting statistics. In most cases the use of the CAM and the FMM_{maj} resulted in age overestimation (Fig. 5). GL14004 was the exception, with all D_e models for this sample resulting in age estimates that are statistically consistent with the 1925 flood (Fig. 5), despite the significant OD (Table 2). The MAM-3 resulted in age estimates that are statistically consistent with the 1918 and 1984 events, however, for the 1925 and 1963 events the MAM-3 underestimates event year (Fig. 5). Given the presence of zero and negative D_e values amongst these modern analogue samples, the MAM-3_{UL} was also applied. It was not possible to fit and calculate error limits for GL14003 and GL14006. However, for GL14001 and GL14004 MAM-3_{UL} produced D_e values significantly less than those from MAM-3, amplifying the underestimation of flood event year (Table S5.2). The tendency for the MAM to underestimate burial ages has been noted by Rodnight et al. (2006), who observed that a small number of young outliers can exert a strong influence on this age model. In contrast, for most of the modern analogue samples, use of the FMM_{min} resulted in age estimates that are consistent with the flood event year (Fig. 5). The only exception is the most recent deposit (GL14001 – 1984 deposit) where age was overestimated.

The ages from the modern analogues indicate that for deposits from the Mfolozi floodplain with positively-skewed, significantly overdispersed inter-grain D_e distributions, the FMM_{min} component appears to be the age model that most consistently identifies the burial dose representative of flood event year. The FMM has the additional benefit of being able to identify multiple dose components, which is particularly useful when post-depositional mixing has occurred within sediments. Therefore, only the FMM and, where OD is <30 %, CAM are used to estimate burial dose from single grain quartz OSL data in this study. For multi-grain D_e measurements, only the CAM is considered, avoiding the identification of phantom dose populations arising from averaging (Arnold et al., 2012).

4.3.2. UCOSP basal flood units

D_r values for the basal samples are lower than those calculated for the known-age samples, with values ranging from 1.52 to 2.06 Gy/ka (Table 4). The two lower-most samples from the UCOSP sequence (GL15119 & GL15120) had Th and U concentrations that were significantly lower than other samples in the sequence. In addition, for GL15119 the U-series appears to be in disequilibrium (Table 4) and the age estimate should be treated with caution.

Four of the five flood units (GL15116-120) encapsulated within the UCOSP basal core produced inter-grain D_e distributions that are positively-skewed and significantly overdispersed (Fig. 6b; Table 2; Fig. S5.2). GL15117 was the exception (Fig. 6a), with an OD of <30 % and the FMM confirming the presence of a single significant dose component ($D_e = 1.33 \pm 0.03$ Gy, p = 92 %). The CAM D_e is adopted for

Table 4
Dosimetry data for UCOSP and Futululu.

Sample	Depth (m)	Grain Fraction (μm)	Moisture Content (%)*	Ge γ-spectrometry (ex-situ)				D_r Components (Gy/ka)			Total D_r (Gy/ka)
				K (%)	Th (ppm)	U (ppm)	$^{226}Ra/^{238}U$	β	γ	Cosmic	
UCOSP Section											
GL14001	0.69	180–250	9	1.77 ± 0.09	7.35 ± 0.48	1.29 ± 0.10	0.86 ± 0.11	1.27 ± 0.26	0.85 ± 0.17	0.18 ± 0.01	2.31 ± 0.31
GL14003	1.55	180–250	6	1.93 ± 0.09	9.98 ± 0.59	1.79 ± 0.11	1.05 ± 0.13	1.51 ± 0.31	1.09 ± 0.22	0.16 ± 0.01	2.76 ± 0.38
GL14004	1.95	180–250	3	1.86 ± 0.09	7.37 ± 0.49	1.13 ± 0.09	0.89 ± 0.14	1.40 ± 0.29	0.91 ± 0.19	0.16 ± 0.01	2.47 ± 0.34
GL14006	3.00	180–250	4	1.96 ± 0.09	6.51 ± 0.46	1.27 ± 0.09	0.90 ± 0.14	1.44 ± 0.30	0.90 ± 0.18	0.14 ± 0.01	2.48 ± 0.35
UCOSP Basal Units											
GL15116	5.15	180–250	11	1.73 ± 0.13	5.93 ± 0.58	1.24 ± 0.15	0.96 ± 0.27	1.19 ± 0.25	0.76 ± 0.16	0.11 ± 0.01	2.06 ± 0.30
GL15117	6.15	180–250	15	1.47 ± 0.12	5.87 ± 0.56	1.07 ± 0.17	0.97 ± 0.23	0.98 ± 0.21	0.66 ± 0.14	0.10 ± 0.01	1.74 ± 0.25
GL15118	6.35	180–250	17	1.59 ± 0.12	6.33 ± 0.59	1.33 ± 0.17	1.03 ± 0.22	1.06 ± 0.22	0.71 ± 0.15	0.09 ± 0.01	1.86 ± 0.27
GL15119	6.75	180–250	11	1.48 ± 0.12	2.41 ± 0.49	0.64 ± 0.13	1.65 ± 0.34	0.93 ± 0.20	0.50 ± 0.11	0.09 ± 0.01	1.52 ± 0.23
GL15120	7.35	180–250	9	1.54 ± 0.12	2.74 ± 0.46	0.63 ± 0.13	1.09 ± 0.13	0.99 ± 0.21	0.53 ± 0.11	0.08 ± 0.01	1.61 ± 0.24
Futululu											
GL15122	0.75	180–250	11	1.74 ± 0.13	7.94 ± 0.64	1.72 ± 0.18	1.09 ± 0.20	1.28 ± 0.27	0.89 ± 0.19	0.18 ± 0.01	2.36 ± 0.33
GL15123	1.67	125–180	16	1.65 ± 0.13	9.09 ± 0.68	2.00 ± 0.19	1.04 ± 0.18	1.27 ± 0.27	0.91 ± 0.19	0.16 ± 0.01	2.34 ± 0.33
GL15124	2.77	90–125	16	1.53 ± 0.12	9.35 ± 0.71	2.07 ± 0.17	1.00 ± 0.15	1.28 ± 0.27	0.90 ± 0.19	0.14 ± 0.01	2.32 ± 0.33
GL15125	2.90	90–125	18	1.65 ± 0.13	9.53 ± 0.70	2.17 ± 0.19	0.95 ± 0.15	1.33 ± 0.28	0.92 ± 0.19	0.14 ± 0.01	2.39 ± 0.34
GL15126	3.82	90–125	22	1.89 ± 0.14	8.40 ± 0.67	1.97 ± 0.19	1.01 ± 0.16	1.37 ± 0.29	0.88 ± 0.18	0.12 ± 0.01	2.37 ± 0.34

* Moisture contents calculated through mass lost by drying, where: $\textit{Moisture content}\ (\%) = \frac{\textit{Wet Mass} - \textit{Dry Mass}}{\textit{Wet Mass}} \times 100$

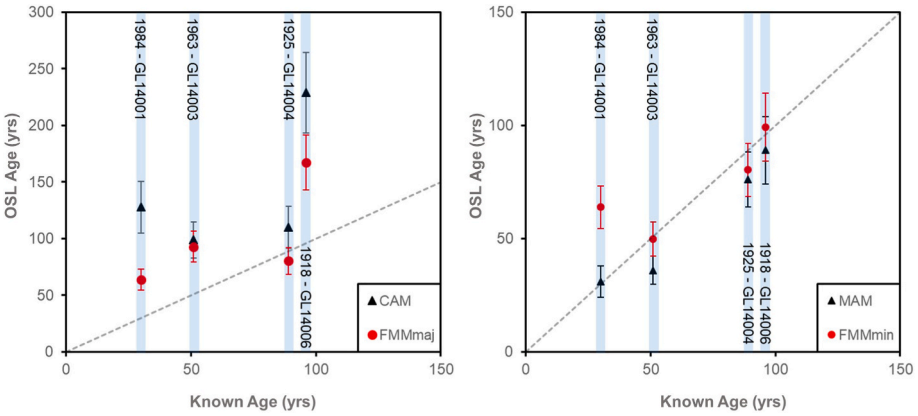

Fig. 5. UCOSP modelled OSL age versus known-age.

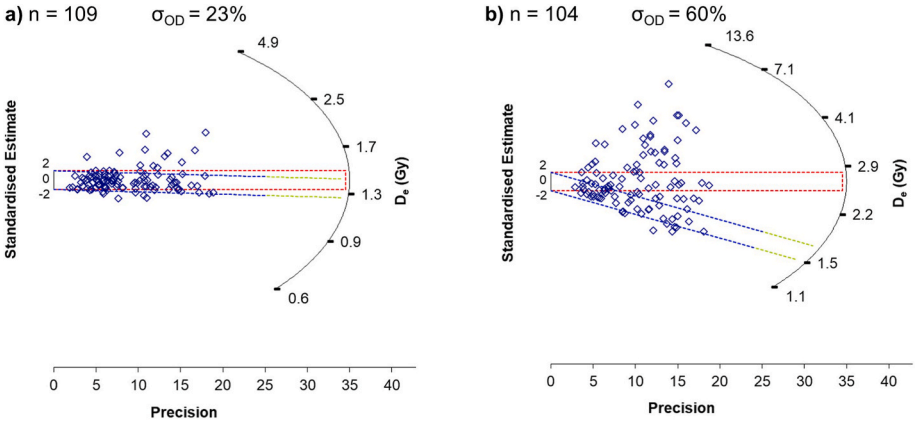

Fig. 6. UCOSP radial plots for a) GL15117 and b) GL15119. Coloured areas represent dose models applied to D_e datasets; the CAM (**red**), the FMM_{min} (**green**) and the FMM_{maj} (**blue**).

GL15117 whilst, given the success in identifying burial doses for the modern analogues, the FMM_{min} is adopted for GL15116 as FMM_{min} and FMM_{maj} are coeval (Fig. S5.2a). The adopted D_e values result in ages of 184 ± 27 and 807 ± 118 yr for GL15116 and GL15117, respectively.

Although partial bleaching is attributed to some of the observed OD for the UCOSP samples given their waterlain origin, further significant contributors are believed to be responsible for the OD observed for GL15118 to GL15120. The influence of partial bleaching upon the mean D_e value is expected to reduce with burial time as residual doses become less significant relative to D_e (Rittenour, 2008). For the UCOSP basal samples the CAM and the FMM_{min} ages diverge with an increase in depth. From GL15117 to GL15120 there is a systematic increase in the difference between the CAM and the FMM_{min} ages, with age discrepancies increasing from 40 to 930 yr. The divergence of ages could be attributed to microdosimetry and the multiplier effect of dose rate with time. In such instances the D_e for grains within low D_r regions becomes further separated from those in high D_r regions with increased burial time. It is then not possible to separate the relative contributions of microdosimetry and partial bleaching within D_e distributions, with the burial dose laying somewhere between the MAM and CAM. Given the complexities associated with these samples, the FMM_{maj} D_e was deemed most appropriate for age calculation as it satisfies most of the D_e population (p = 36–49 %; Table S5.1). For GL15119 and GL15120 the FMM_{maj} and the FMM_{min} are the same dose component. Ages of 1.09 ± 0.17, 1.04 ± 0.24 and 1.58 ± 0.24 ka are calculated for GL15118, GL15119 and GL15120 respectively. All ages satisfy stratigraphic consistency, however, each estimate should be used cautiously given the complexities associated with both D_e and D_r.

4.3.3. *Fututulu*

The Futululu samples display minimal variation in D_r (Table 4), all values are statistically consistent with mean D_r ranging from 2.32 to 2.39 Gy/ka. Minimal variability is observed in estimated radionuclide concentration and most values are statistically consistent. All $^{226}Ra/^{238}U$ ratios fall within 10 % of unity, suggesting the absence of significant U-series disequilibrium.

Single-grain analysis was undertaken upon two samples from the Futululu sequence, GL15122 and GL15123. GL15122 was the uppermost sample from the sequence, producing minimal skew in its inter-grain D_e distribution, CAM, FMM_{min} and FMM_{maj} D_e values that are statistically consistent, and an OD <30 % (Table 2; Fig. S6.1a). Collectively, this suggests GL15122 was well-bleached upon deposition and has remained undisturbed following burial. The D_e distribution for GL15123 has significant OD (39 %), driven by the incorporation of numerous high-dose values (Fig. S6.1b). This produced a distribution with a strong positive skew and a slight high-dose tail, however, the CAM and the FMM_{min} results are statistically consistent (Table 2). The CAM was adopted and produced ages of 214 ± 30 and 218 ± 32 yr for GL15122 and GL15123, respectively.

GL15124, GL15125 and GL15126 were taken from the earliest material deposited at the Futululu site. Despite isolating the fine sand quartz fraction, multi-grain aliquots were used for D_e analysis as it was not possible to confirm that only a single grain of 90–125 μm quartz was situated in each measurement position. Ages calculated using the CAM are statistically consistent and represent three closely spaced depositional events occurring between 1.89 and 2.10 ka (Table 2).

4.3.4. South Lake

Fig. 7 provides an overview of the key variables used for South Lake D_r calculation. Average D_r values range from 1.64 to 2.67 Gy/ka and have associated errors of 12–15 % (Table 3), with core compaction and subsequent γ-modelling (Table S3.1) contributing to the overall uncertainty. Despite the variability in $^{226}Ra/^{238}U$ throughout the sequence, all ratios fall within 0.5 of unity (Fig. 7) suggesting U-series disequilibria should not present a significant issue.

4.3.4.1. Unit 1 (4.78–2.85 m). Five sand-based flood deposits were dated within unit 1 (GL15025-32) using single-grain OSL, with two samples (upper and lower) processed for each of the three thickest deposits (GL15026–27, GL15028-29 & GL15030-31) to attempt to evaluate whether they represented a single depositional phase. Partial bleaching does not appear to be an issue with unit 1 samples (GL15025 to GL15032) as all single-grain D_e distributions are unimodal, near symmetrical and have similarly low inter-grain D_e OD ranging between 21 and 24 % (Fig. 8b; Fig. S7.1f – S7.1m; Table 3). The CAM is most appropriate for age calculation and central D_e values range from 9.40 to 14.44 Gy, resulting in depositional ages that span from 5.24 ± 0.73 to 7.15 ± 1.02 ka. All depositional ages are consistent with their relative stratigraphic positions (Table 3). A radiocarbon sample (SL_AMS_5; Table 1) from the boundary of unit 1 and 2 dates this part of the sequence to 4.73 ± 0.14 cal ka BP, which is statistically consistent with the uppermost OSL sample from unit 1 (GL15025; 5.24 ± 0.73 ka) and supports the upper OSL age limit.

4.3.4.2. Unit 2 (2.85–1.48 m). Two single-grain (GL15023 & GL15024) and three fine silt (GL15020-22) age estimates were calculated from unit 2. The lowermost sample from unit 2 (GL15024) displayed minimal D_e OD (22 %) and modelled ages were statistically indistinct (Table 3; Fig. S7.1e). GL15024 displayed a significant increase in skewness relative to the samples in unit 1 (Table 3), driven by a small number of high-dose grains. Given the minimal OD and the consistency observed between dose models, GL15024 appears well-bleached and the CAM results in a depositional age (3.58 ± 0.49 ka) that satisfies stratigraphic consistency relative to ages in unit 1.

GL15023 was also collected from a well-preserved sand bed in unit 2 and produced a D_e distribution with a higher OD (42 %) relative to samples from greater depth (Fig. 8a; Fig. S7.1). The FMM_{min} D_e is statistically distinct relative to the CAM (Table 3), indicating partial bleaching and/or microdosimetry could have had a significant influence upon D_e distribution. For most modern analogue samples, the FMM_{min} component resulted in calculation of the most appropriate age, with the D_e situated between the MAM and the CAM results. Given these findings, $FMM_{k=2}$ was selected as a D_e estimate for GL15023, encapsulating 24 % of grains and resulting in an age of 3.78 ± 0.57 ka. The age is statistically consistent with GL15024, and the modelled D_e is situated between the MAM (Fig. S7.1d) and the CAM (Fig. 8a).

The remaining OSL ages from unit 2 are all based on multi-grain aliquots of fine silt quartz, owing to the absence of fine sand at this level. GL15022 produced a stratigraphically consistent central age (1.85 ± 0.23 ka; Table 3) that is less than single-grain ages situated lower in the sequence and greater than a radiocarbon age (SL_ AMS_3A; 1.39 ± 0.02 cal ka BP; Table 1) taken 9 cm above the OSL sample. The final two fine silt ages from unit 2 (GL15020 and GL15021) were situated above SL_AMS_3A and produced central ages (3.67 ± 0.47 & 3.47 ± 0.43 ka; Table 3) that are significantly greater than SL_ AMS_3A and GL15022.

4.3.4.3. Unit 3 (1.48–0.76 m). Only one fine silt OSL sample (GL15016) was isolated from unit 3, it was taken from a clastic lamination at the top of the unit and produced a central age of 2.81 ± 0.36 ka (Table 3), which pre-dates GL15022 and SL_ AMS_3A. The age for GL15016 is also significantly greater than two further radiocarbon ages (SL_AMS_1 & _AMS_2; Table 1) taken from the lower portions of unit 3 dated to 1.19 ± 0.06 and 1.30 ± 0.05 cal ka BP.

4.3.4.4. Unit 4 (0.76–0.00 m). Unit 4 is formed of the uppermost material from the South Lake sequence. GL16099 was collected from the base of the unit, and its central age estimate (1.55 ± 0.19 ka) is stratigraphically consistent with OSL samples GL15022 to GL15032 (Table 3). However, it pre-dates the radiocarbon ages produced for unit 3 and may be considered a maximum age for unit 4 deposition.

The remaining three samples from unit 4 are near-surface, single-grain ages which were taken from 0.48 m upwards. Samples GL15015, GL15158 and GL15157 are interpreted simultaneously given their similar characteristics. GL15015 was collected from a distinct sand lense whilst the prevalence of sand was less obvious for GL15157 and GL15158. All single-grain D_e distributions for the near-surface samples are significantly overdispersed, positively skewed (Table 3) and, other

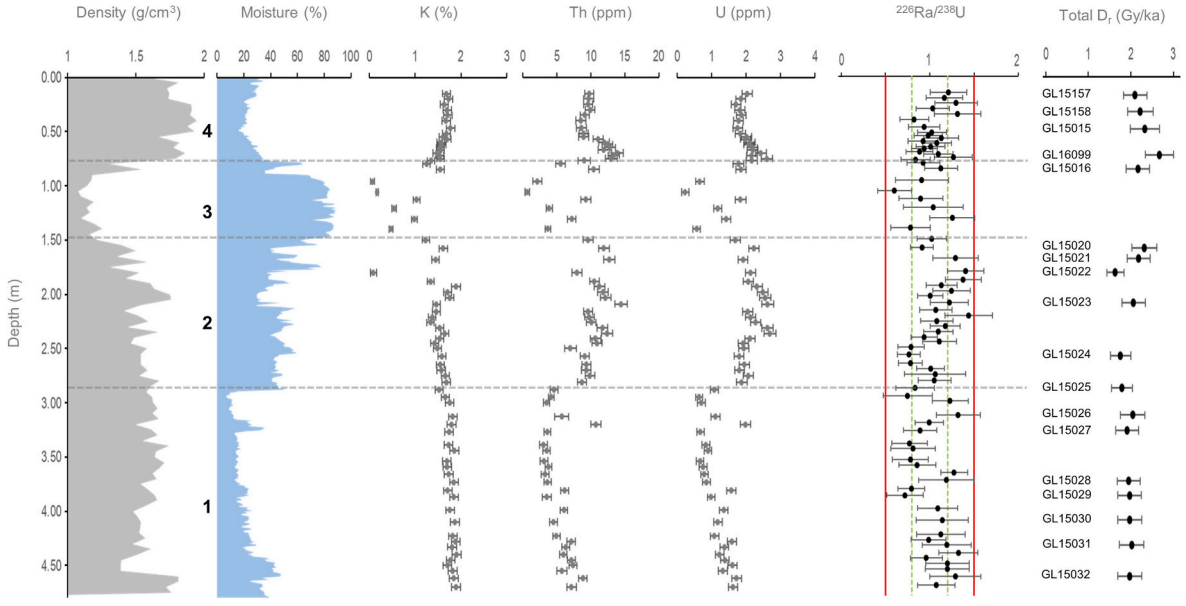

Fig. 7. Key variables used for South Lake γ-modelling and D_r calculation. $^{226}Ra/^{238}U$ ratios are presented for assessment of U-series disequilibria - 20 % (green/dashed line) and 50 % (red/solid line) margins highlighted.

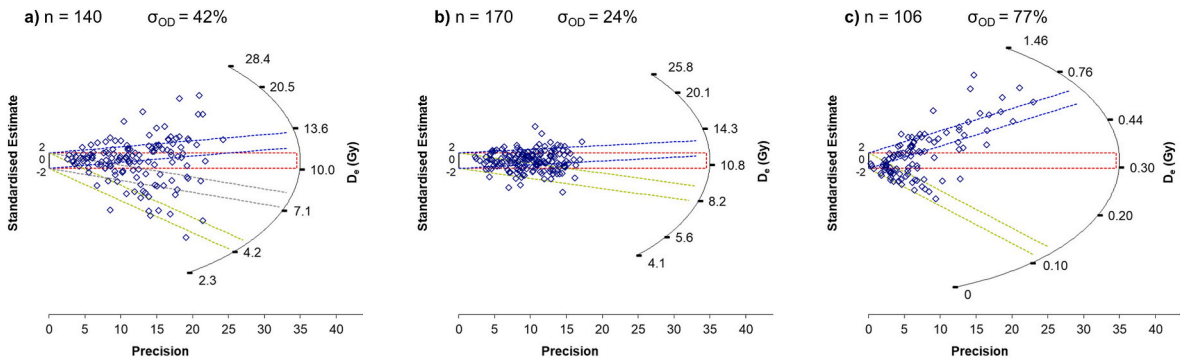

Fig. 8. Example South Lake radial plots for a) GL15023, b) GL15028 and c) GL15158. Coloured areas represent the; CAM (**red**), FMM_{min} (**green**), FMM_{maj} (**blue**) and for GL15023, $FMM_{k=2}$ (**grey**).

than the UCOSP modern analogues, are the only other samples in this study that feature zero and negative dose grains (3–5 %). Recent reworking (i.e. pedoturbation) is suggested as a potential contributor to the observed distributions owing to the presence of zero-dose grains and the proximity of the samples to the surface (Gliganic et al., 2016).

For the three near-surface samples, two distinct D_e populations (*c.* 0.1 & 0.6 Gy; Table 3; Fig. 8c; Fig. S7.1a – S7.1c) are interpreted as representing separate depositional events. Given the increase with depth in the proportion of grains falling within the FMM_{maj} dose component (Table S7.1), this is selected for age calculation of the deepest of the three samples (GL15015; 268 ± 41 yr). This represents the dominant D_e population and the deposition of the well-preserved sand lense. Samples GL15157 and GL15158 are believed to represent recent phases of deposition and reworking, potentially caused by flood intrusions onto the basin, the FMM_{min} result (54 ± 8 yr) is likely the most suitable age bracket for these.

4.4. Bayesian age-depth modelling

Each of the chronologies in this study was subject to Bayesian analysis using the P_Sequence model in OxCal (v4.2; Bronk Ramsey, 2009). The deposition models for each site (Fig. 9) displayed good overall agreement (69.4–101.3 %) and the relative errors associated with OSL age estimates were reduced by between 1 and 9 %. Unmodelled ages were adjusted by between 1 and 23 %, with the greatest adjustments being experienced by the UCOSP and South Lake samples. Further details on the modelling are provided in the supplementary material (S8).

For the South Lake sequence interpolation of the 1σ fitting was used to produce temporal constraints for each of the stratigraphic units (Table 5). In addition, an OSL age could not be produced for a thin clastic band within unit 3 at 1.13 m owing to limited sample mass – interpolation produced an age of 1.26 ± 0.04 ka. Furthermore, interpolation can be used to assess the scale of age overestimation for the fine silt ages omitted from the deposition model. Interpolated ages for GL15016 (1.24 ± 0.04 ka), GL15020 (1.38 ± 0.03 ka) and GL15021 (1.50 ± 0.14 ka) indicate that fine silt samples overestimate age by c. 1.60 to 2.30 ka (127–166 %).

5. Discussion

5.1. Floodplain chronostratigraphy

5.1.1. UCOSP

The avulsion fan sediments preserved in the UCOSP sequence featured an alternation of fine grain material (silt and clays; Fig. 9a) and fine-medium sands. Given the rapidly aggrading floodplain setting, lack

Table 5
Interpolated ages for sedimentary units identified for the South Lake sequence (*Bayesian model did not extend to contemporary surface).

Unit	Depth (m)	Interpolated Age (years)	
		Maximum	Minimum
1	4.62–2.85	7249 ± 537	4906 ± 252
2	2.85–1.48	4906 ± 252	1347 ± 44
3	1.48–0.76	1347 ± 44	1212 ± 50
4	0.76 - Surface	1212 ± 50	54 ± 8*

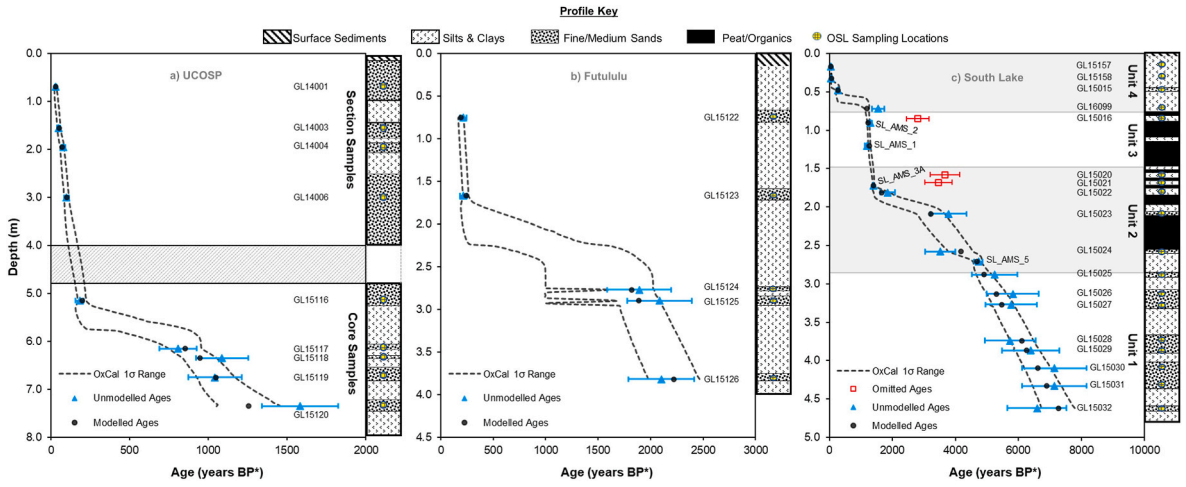

Fig. 9. Bayesian deposition models for a) UCOSP, b) Futululu and c) South Lake.

of organic material and insufficient time between flood events for soil development, sand units are interpreted as the initial flood/avulsion event deposits whilst the units comprising fine grain material overlay these and represent the waning stages of flooding. As such, each large flood event preserved in the UCOSP sequence displays a pattern of upward fining and features a lower sand and upper silt and clay component. In total, nine flood events are recorded within the sequence with the four most recent being of known age, occurring in AD 1918, 1925, 1963 and 1984.

The chronology for UCOSP displays two periods of significant flooding for the central floodplain. Between *c.* 1.26 ka and 850 yr four deposition events are recorded by the sequence with ages centred on 1.26 ± 0.21, 1.05 ± 0.12 ka, 946 ± 110 and 854 ± 106 yr (Fig. 9a), following these floods there is a *c.* 600-year hiatus. Another period of increased flooding initiates at 200 yr and spans to the present day. There are five flood units for this period, including the four known age events plus an additional flood event at 200 ± 26 yr.

5.1.2. Futululu

The Futululu sequence represents the development of a crevasse splay feature which had encroached into the blocked-valley lake basin via a drainage channel. The sequence was formed predominantly of silt and clay units, but it also featured five fine/medium sand-based beds (Fig. 9b). These sediments are interpreted as representing a similar pattern of flood-driven sedimentation as the UCOSP site, with sand beds representing the initial flood intrusions and the finer material representing the waning stages of flood events.

Two periods of increased flooding are also observed for the Futululu sequence. The three earliest flood events occurred at 2.22 ± 0.25, 1.89 ± 0.20 and 1.82 ± 0.22 ka, following which there is a *c.* 1.6 ka hiatus where no flood intrusions are recorded (Fig. 9b). After the hiatus two further flood events are detected at 241 ± 27 and 195 ± 26 yr. The flood chronology indicates that encroachment of the crevasse splay into the Futululu basin involved two depositional phases.

5.1.3. South Lake

The South Lake sequence extends back to 7.2 ka, encapsulating the full development of the blocked-valley lake. The sedimentology reveals four distinct units (1–4; Fig. 9c) representing different phases of deposition. Unit 1 represents the earliest phase of deposition and contains five sand beds preserved amongst clay rich sediments. The deposition of sand beds initiated in the early-Holocene at 7.2 ± 0.5 ka and continued until 4.9 ± 0.3 ka, with ages for the three intervening sand beds centred on 6.8 ± 0.4, 6.2 ± 0.4 and 5.4 ± 0.3 ka (Fig. 9c). This phase of deposition probably precedes the formation of the blocked-valley lake basin when the site was still connected to the mainstem river. Given the connectivity to the mainstem at this time, we interpret the sand beds in unit 1 as representing distinct large flood events that affected the floodplain. Nearby at Lake Teza (Fig. 1), Neumann et al. (2010) observed an abrupt increase in sedimentation at 6.5 ka and suggested a possible cause was tropical cyclones and floods. More recently, Green et al. (2022) identified a period of intense storm activity along the eastern coast of South Africa between 7.0 and 4.8 ka. These studies complement our interpretation of the lower sand beds and indicate that the Mfolozi floodplain was likely impacted by large storm and flood events at this time.

The timing of unit 1 sedimentation coincides with rising sea levels on the South African coast, with a mid-Holocene highstand occurring between 6.5 and 5.5 ka (Cooper et al., 2018). During this period the Mfolozi floodplain experienced a switch from river incision to aggradation owing to the higher base level created by rising sea levels. The sand beds in unit 1 represent this initial phase of aggradation across the floodplain which is characterised by the fluvial reworking and deposition of aeolian sands (Grenfell et al., 2010). The aeolian nature of the reworked sediments probably contributed to the observed D_e distributions and minimal OD (21–24 %; Table 3) for the sand beds in unit 1, the sediments were likely well-bleached before being mobilised and deposited by floodwaters.

From 4.7 ± 0.1 ka organic matter started to accumulate at the South Lake site marking the shift from a fluvial to lacustrine/peatland environment and the initial formation of the blocked-valley lake basin (unit 2; Fig. 9c). The timing of formation closely corresponds to other observations upon the floodplain, including the *c.* 4.5 ka initiation of tributary impoundment for Lake Futululu (Grenfell et al., 2010) and the development of a freshwater-dominated environment in the adjacent Lake Teza (4.7 ka; Neumann et al., 2010). Following formation, the South Lake basin preserved an alternating pattern of organic and clastic deposition until 1.35 ± 0.04 ka. It is likely that the accumulation of peat and organics occurred when the basin was relatively isolated from clastic input by the mainstem river. These clastic bands, composed predominantly of silt or fine/medium sands, are interpreted as flood deposits. Two sand-based flood units were deposited at 4.17 ± 0.40 and 3.21 ± 0.50 ka, whilst flood units formed of silt were deposited at 1.66 ± 0.26, 1.50 ± 0.14 and 1.38 ± 0.03 ka (Fig. 9c). The two earliest of the silt flood units are consistent with ages produced for flood events (1.70 and 1.47 ka) identified at Lake Futululu by Grenfell et al. (2010).

Following 1.35 ka, there was a short phase (*c.* 100 yr) of heightened organic accumulation at South Lake with minimal clastic input (Unit 3; Fig. 9c). Two flood intrusions onto the basin are recorded as silt units within the sedimentology (1.13 and 0.85 m) during this short phase, occurring at 1.26 ± 0.04 and 1.24 ± 0.04 ka.

At 1.21 ± 0.05 ka South Lake experienced another abrupt change, marked by a significant drop in the accumulation of organics and the deposition of clastic sediment (unit 4; Fig. 9c). The deposition of clastic-rich sediment continues until the present day with evidence of three flood deposits comprising fine sands occurring at 268 ± 41, 58 ± 7 and 52 ± 7 yr.

5.2. Optical dating of blocked-valley lake deposits

The analysis completed for the South Lake site addresses the first of the two inter-related aims of this study - to evaluate OSL as a technique for dating clastic flood sediments preserved within blocked-valley lake deposits. The least equivocal aspect of chronicling the South Lake sequence was the single-grain dating of basal sands (GL15025-GL15032) which represented 5 phases of fluvial reworking and deposition between 7.2 and 4.9 ka (Fig. 9c). Single-grain D_e distributions displayed minimal OD (≤24 %; Table 3; Fig. S7.1f – S7.1m) and were suited to the CAM. In addition, the sedimentology displayed similar variations resulting in statistically consistent D_r values (Table 3; Fig. 7). Ages produced for the sand-beds displayed stratigraphic consistency and agreement with radiocarbon ages.

The dating of sediments deposited after the formation of the blocked-valley lake basin displayed varying degrees of success. Single-grain OSL ages exhibited stratigraphic consistency and broad agreement with radiocarbon ages. Single-grain D_e distributions varied, with OD ranging from 22 to 86 % (Table 3) and some samples requiring D_e modelling. Most known-age deposits at the UCOSP site indicated that the FMM was best suited to isolating an appropriate D_e for heterogeneously bleached Mfolozi sediments (Fig. 5). The most suited FMM dose components typically fell between the MAM and the CAM (Table 2). Based on the observations from the UCOSP site, the FMM was applied to over-dispersed single-grain D_e distributions from South Lake. The consistency of age estimates suggests that, despite the requirement for D_e modelling, single-grain OSL is suitable for use within blocked-valley lake deposits.

Ages produced using fine silt multi-grain aliquots were less successful; three of the five samples analysed for the South Lake sequence significantly overestimated age and did not align with radiocarbon and single-grain OSL ages. This is not a unique observation and in a previous comparison of coarse- and fine-grain OSL ages produced for fluvial terraces, fine silt aliquots tended to overestimate age by up to a factor of ten (Thompson et al., 2018). In the case of South Lake, it is suggested

that fine silt OSL age overestimation stems from aliquot size and incomplete bleaching, particularly given the cohesive nature of the sediments and their waterlain origin. A fine silt quartz aliquot can include around one million grains and any D_e variability caused by partial bleaching is not detectable because of averaged signals (Duller, 2008).

In most instances, the D_r calculated for fine silt samples was either similar to or greater than that calculated for fine sand samples within the sequence (Table 3; Fig. 7). Whilst a higher D_r is expected for the fine silt fraction, given the additional α-component and the lower β attenuation, the calculated D_r would have to at least double to align the fine silt age estimates with other ages in the sequence. This seems unlikely, especially given that most of the fine silt units are surrounded by saturated sediments (moisture content; Fig. 7) with an elevated (>20 %) organic content (Fig. 3). This further indicates that overestimation is rooted in D_e. The fine silt age estimates produced here suggest that OSL is not well-suited for dating blocked-valley lake deposits. These ages should be interpreted cautiously and, where possible, in combination with single-grain OSL and radiocarbon dating. For this study, interpolation of a Bayesian deposition model comprised of single-grain OSL and radiocarbon ages appears the best solution for obtaining the age of fine silt flood units preserved within organic-rich sediment.

From the outset, two predominant factors were likely to cause issues for successful OSL dating of blocked-valley lake sediments. The first being the waterlain nature of samples and the likelihood of partial bleaching. In this study it has been demonstrated that by using single-grain quartz OSL it is possible to identify partial bleaching using D_e distribution methods and make accommodations through dose modelling, more specifically the FMM. However, for fine silt OSL dating the combination of signal averaging (caused by aliquot size) and partial bleaching results in age overestimation. The second factor concerns D_r and the complexity of the sedimentology. The significant fluctuations in organic and moisture content, plus the distinct changes in the clastic sediment matrix required careful consideration when calculating D_r. By conducting density and γ modelling (Fig. S3.1; Table S3.1) representative D_r values appear to have been calculated for all age estimates, contributing to their stratigraphic consistency. Whilst this does not act as a replacement for *in situ* gamma-spectrometry, it provides a useful alternative when on-site measurements are not possible.

5.3. Palaeoenvironmental implications

The palaeoflood chronologies produced for the Mfolozi River floodplain in this study provide the first long-term flood record for the east coast of South Africa, offering an opportunity to investigate connections between flood frequency and long-term palaeoclimate shifts in the region. Multiple sedimentary records from the eastern coast of South Africa provide evidence for substantial Holocene variability in the local hydrological regime (Humphries et al., 2016, 2019, 2020, 2024; Miller et al., 2019). These fluctuations have been interpreted as a response to intensified El Niño activity, leading to episodes of pronounced regional drought.

A sedimentary record from Lake Muzi situated on the Mkhuze River floodplain ~95 km north of the Mfolozi sampling sites (Humphries et al., 2019), offers a particularly useful comparison for contextualising the palaeofloods identified in this study. Muzi represents a blocked-valley lake that is primarily sustained by groundwater inputs, but receives water and sediment from the Mkhuze River when high flows result in bank overspill. Sediment accumulation within Lake Muzi is characterised by distinct layering of finely-grained carbonate horizons within silt-dominated deposits (Fig. 10a) that are interpreted to reflect shifts between the supply of fluvial sediment during relatively wet periods and the *in situ* precipitation of calcium carbonate that occurs during periods of prolonged aridity (Humphries et al., 2019). Comparison between palaeoflood events identified on the Mfolozi River floodplain and sedimentary evidence from Lake Muzi reveals a temporal correspondence between multiple flood events and the onset of significant clastic deposition within the Lake Muzi basin (Fig. 10a). This synchronicity suggests that extreme flooding events on the Mfolozi floodplain were likely triggered by climatic dynamics affecting the broader region.

Previous work on the Mfolozi floodplain suggests that overbank flood deposits formed of silts are indicative of normal flooding whilst coarser sand units can be attributed to larger flood events (Grenfell et al., 2009). Although such an interpretation should be treated with caution given potential complexities arising from variability in sediment source and availability, as well as the propensity of the Mfolozi River to avulse during large flood events, it is notable that several sandy flood deposits identified in the South Lake record often coincide with the most pronounced periods of clastic accumulation recorded at Lake Muzi (Fig. 10a). The most prominent of these synchronous events are dated to 4.9 ± 0.3 and 4.2 ± 0.4 ka. The flood event at 3.2 ± 0.5 ka appears to be an exception, potentially reflecting a localised precipitation event that primarily affected the Mfolozi River catchment, with limited impact on the Mkhuze River system.

Several silt-dominated flood deposits identified in the Mfolozi record (e.g., 1.7 and 1.5 ka events) are not evident in the Lake Muzi sequence (Fig. 10a; Humphries et al., 2019). This discrepancy may reflect the lower magnitude of these events or differential sensitivity of the two depositional environments to recording past environmental changes. Despite these differences, it is notable that a cluster of flood events around 1.2 ka on the Mfolozi River floodplain coincides with the onset of significant clastic accumulation at Lake Muzi (Fig. 10a). Overall, considering inherent dating uncertainties and the variable sensitivity of sedimentary archives to flood magnitude, the observed temporal alignment between Mfolozi palaeoflood events and sedimentation at Lake Muzi suggests a potential common climatic driver.

Dramatic shifts in hydroclimate over the mid-late Holocene in northern KZN have been attributed to ENSO variability and its influence on moisture convergence over the eastern region of South Africa. Using independent sedimentary evidence from three sites in northern KZN, Humphries et al. (2024) developed a composite proxy record of regional drought (Fig. 10b). This record reveals several major drought episodes spanning multi-centennial to millennial timescales, demonstrating a statistically significant correlation with reconstructed El Niño activity from Laguna Pallcacocha, Ecuador (Moy et al., 2002), a widely recognised and robust global archive of Holocene ENSO variability (Hagemans et al., 2021; Mark et al., 2022). Comparison of the Mfolozi flood chronologies with this composite drought record indicates that flood events on the Mfolozi River floodplain predominantly occurred during inter-drought periods associated with weakened El Niño activity (i.e., La Niña or neutral ENSO phases; Fig. 10b).

Present-day summer rainfall variability in the region is strongly connected to ENSO, primarily through its influence on moisture conveyed from the southwest Indian Ocean. La Niña conditions produce cyclonic circulation anomalies that enhance convective rainfall across southern Africa, increasing the probability of extreme rainfall events during these periods (Kruger, 1999; Rapolaki et al., 2019). The results of this study suggest that similar changes in ENSO activity during the mid-to-late Holocene likely played an underlying role in triggering extreme flooding along the east coast of South Africa.

6. Conclusion

Quartz OSL is a useful technique for dating clastic flood sediments preserved within blocked-valley lake profiles, however, the success of the technique is dependent on aliquot size. It is advised that, where possible, single-grain D_e analysis upon sand-sized quartz should be conducted to isolate representative burial doses, with resultant single-grain ages also ratified by independent age controls. Where there is a combination of a high organic content and dominance of fine silt within the clastic matrix, fine silt OSL ages appear to overestimate age and should be treated with caution. Interpolation of deposition models

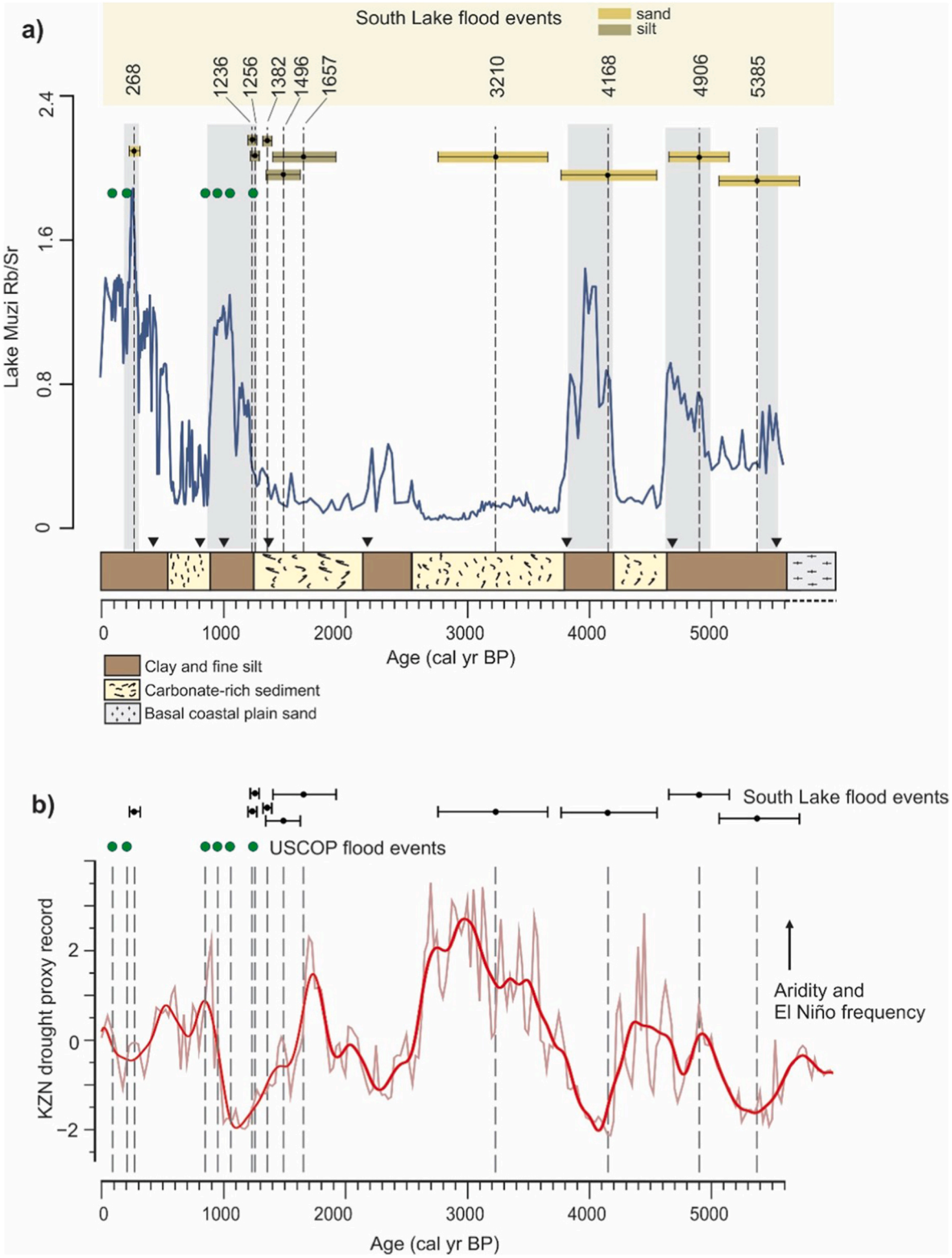

Fig. 10. a) Comparison between palaeoflood events identified at South Lake and USCOP sites on the Mfolozi River floodplain (this study) and record of fluvial deposition (Rb/Sr) at Lake Muzi on the Mkhuze River floodplain (Humphries et al., 2019). USCOP flood events are indicated by green dots. Grey shading highlights periods when South Lake palaeoflood events coincide or mark the onset of significant clastic deposition at Lake Muzi. Radiocarbon age control points used in the development of the Lake Muzi age-depth model are indicated by black triangles. b) The composite drought record developed for the east coast of South Africa, providing evidence for the occurrence of several major drought events and interpreted to reflect the regional hydroclimatic response to the most prominent, low-frequency features of ENSO (Humphries et al., 2024). A comparison with Mfolozi flood chronologies indicates that extreme flood events generally occurred during inter-drought periods characterised by weakened El Niño activity.

constructed using single-grain OSL and radiocarbon age estimates from surrounding sediments provides a useful alternative when fine silt OSL misrepresents depositional age.

This study has generated the first long-term flood record for the east coast of South Africa, providing new insights into the drivers of extreme flooding in the region. Comparison between Mfolozi palaeoflood chronologies and independent sedimentary hydroclimatic evidence from the region suggests a historical tendency for extreme floods to occur more frequently during weakened El Niño conditions (i.e., La Niña or neutral ENSO phases). This suggests that variations in ENSO activity through the mid-to-late Holocene likely played a fundamental role in triggering extreme flooding along South Africa's east coast. Understanding the behaviour of ENSO under projected climate change is thus critical for assessing and mitigating future flood risks in the region.

CRediT authorship contribution statement

Jamie C. Wood: Writing – review & editing, Writing – original draft, Visualization, Resources, Project administration, Methodology, Investigation, Funding acquisition, Formal analysis, Data curation, Conceptualization. **Phillip S. Toms:** Writing – review & editing, Supervision, Resources, Project administration, Methodology, Investigation, Funding acquisition, Conceptualization. **Michael C. Grenfell:** Writing – review & editing, Supervision, Resources, Project administration, Methodology, Investigation, Funding acquisition, Conceptualization. **Marc S. Humphries:** Writing – review & editing, Visualization, Resources, Methodology, Investigation, Formal analysis, Data curation, Conceptualization.

Role of funding source

This research was conducted as part of a PhD project funded by a University of Gloucestershire Studentship. Fieldwork was supported by funding from the British Society for Geomorphology (BSG), Quaternary Research Association (QRA) and The Dudley Stamp Memorial Award (Royal Geographical Society with IBG).

Declaration of competing interest

The authors declare that they have no known competing financial interests or personal relationships that could have appeared to influence the work reported in this paper.

Acknowledgements

We would like to thank Prof. Fred Ellery for his assistance in the field and Prof Spike McCarthy for lending us the vibracorer. Dr Jemma Finch and Salona Reddy for their initial analysis on pollen and charcoal, plus the funding provided to secure two further radiocarbon dates. The iSimangaliso Wetland Park Authority and The Umfolozi Sugar Mill for granting access to field sites. We would also like to thank Svenja Riedesel and one anonymous reviewer for their comments and suggestions that improved the original manuscript.

Appendix A. Supplementary data

Supplementary data to this article can be found online at https://doi.org/10.1016/j.quaint.2025.110101.

References

Aitken, M.J., 1985. Thermoluminescence Dating. Academic Press, London.
Arnold, L.J., Demuro, M., Navazo Ruiz, M., 2012. Empirical insights into multi-grain averaging effects from 'pseudo' single-grain OSL measurements. Radiat. Meas. 47 (9), 652–658. https://doi.org/10.1016/j.radmeas.2012.02.005.
Arnold, L.J., Roberts, R.G., 2009. Stochastic modelling of multi-grain equivalent dose (De) distributions: implications for OSL dating of sediment mixtures. Quat. Geochronol. 4 (3), 204–230. https://doi.org/10.1016/j.quageo.2008.12.001.
Arnold, L.J., Roberts, R.G., Galbraith, R.F., DeLong, S.B., 2009. A revised burial dose estimation procedure for optical dating of young and modern-age sediments. Quat. Geochronol. 4 (4), 306–325. https://doi.org/10.1016/j.quageo.2009.02.017.
Blake, D.H., Ollier, C.D., 1971. 'Alluvial plains of the Fly River, Papua'. Z. Geomorph. N. F. 12, 1–17.
Bøtter-Jensen, L., Bulur, E., Duller, G.A.T., Murray, A.S., 2000. Advances in luminescence instrument systems. Radiat. Meas. 32 (5–6), 523–528. https://doi.org/10.1016/S1350-4487(00)00039-1.
Brennan, B.J., 2003. Beta doses to spherical grains. Radiat. Meas. 37 (4–4), 299–303. https://doi.org/10.1016/S1350-4487(03)00011-8.
Bronk Ramsey, C., 2009. Bayesian analysis of radiocarbon dates. Radiocarbon 51 (1), 337–360. https://doi.org/10.1017/S0033822200033865.
Cooper, J.A.G., Green, A.N., Compton, J.S., 2018. Sea-level change in southern Africa since the last glacial maximum. Quat. Sci. Rev. 201, 303–318. https://doi.org/10.1016/j.quascirev.2018.10.013.
Cunningham, A.C., Wallinga, J., 2012. Realizing the potential of fluvial archives using robust OSL chronologies. Quat. Geochronol. 12, 98–106. https://doi.org/10.1016/j.quageo.2012.05.007.
Duller, G.A.T., 2008. Single-grain optical dating of Quaternary sediments: why aliquot size matters in luminescence dating. Boreas 37 (4), 589–612. https://doi.org/10.1111/j.1502-3885.2008.00051.x.
Duller, G.A.T., Bøtter-Jensen, L., Kohsiek, P., Murray, A.S., 1999a. A high sensitivity optically stimulated luminescence scanning system for measurement of single sand-size grains. Radiat. Protect. Dosim. 84 (1–4), 325–330. https://doi.org/10.1093/oxfordjournals.rpd.a032748.
Duller, G.A.T., Bøtter-Jensen, L., Murray, A.S., Truscott, A.J., 1999b. Single grain laser luminescence (SGLL) measurements using a novel automated reader. Nucl. Instrum. Methods Phys. Res. Sect. B Beam Interact. Mater. Atoms 155 (4), 506–514. https://doi.org/10.1016/S0168-583X(99)00488-7.
Dunn, J.H., Alexander, L.V., Donat, M.G., Zhang, X., Bador, M., Herold, N., Lippmann, T., Allan, R., Aguilar, E., Barry, A.A., Brunet, M., Caesar, J., Chagnaud, G., Cheng, V., Cinco, T., Durre, I., de Guzman, R., Htay, T.M., Ibadullah, W.M.W., Ibrahim, M.K.I. B., Khoshkam, M., Kruger, A., Kubota, H., Leng, T.W., Lim, G., Li-Sha, L., Marengo, J., Mbatha, S., McGree, S., Menne, M., de los Milagros Skansi, M., Ngwenya, S., Nkrumah, F., Oonariya, C., Pabon-Caicedo, J.D., Panthou, G., Pham, C., Rahimzadeh, F., Ramos, A., Salgado, E., Salinger, J., Sané, Y., Sopaheluwakan, A., Srivastava, A., Sun, Y., Timbal, B., Trachow, N., Trewin, B., van der Schrier, G., Vazquez-Aguirre, J., Vasquez, R., Villarroel, C., Vincent, L., Vischel, T., Vose, R., Yussof, M., 2020. Development of an updated global land in situ-based data set of temperature and precipitation extremes: HadEX3. JGR Atmosph. 125 (16). https://doi.org/10.1029/2019JD032263.
Durcan, J.A., Duller, G.A.T., 2011. The fast ratio: a rapid measure for testing the dominance of the fast component in the initial OSL signal from quartz. Radiat. Meas. 46 (10), 1065–1072. https://doi.org/10.1016/j.radmeas.2011.07.016.
Engelbrecht, C.J., Engelbrecht, F.A., Dyson, L.L., 2013. High-resolution model-projected changes in mid-tropospheric closed-lows and extreme rainfall events over southern Africa. Int. J. Climatol. 33 (1), 173–187. https://doi.org/10.1002/joc.3420.
Finlayson, B., Kenyon, C., 2007. Lake Nuga nuga: a levee-dammed Lake in central Queensland, Australia. Geogr. Res. 45 (3), 246–261. https://doi.org/10.1111/j.1745-5871.2007.00458.x.
Galbraith, R.F., 2005. Statistics for Fission Track Analysis. Chapman & Hall, London.
Galbraith, R.F., Green, P.F., 1990. 'Estimating the component ages in a finite mixture'. Int. J. Radiat. Appl. Instrum. Nucl. Tracks Radiat. Meas. 17 (3), 197–206. https://doi.org/10.1016/1359-0189(90)90035-V.
Galbraith, R.F., Roberts, R.G., 2012. Statistical aspects of equivalent dose and error calculation and display in OSL dating: an overview and some recommendations. Quat. Geochronol. 11, 1–27. https://doi.org/10.1016/j.quageo.2012.04.020.
Galbraith, R.F., Roberts, R.G., Laslett, G.M., Yoshida, H., Olley, J.M., 1999. Optical dating of single and multiple grains of quartz from Jinmium rock shelter, Northern Australia: part I, experimental design and statistical models. Archaeometry 41 (2), 339–364. https://doi.org/10.1111/j.1475-4754.1999.tb00987.x.
Gliganic, L.A., Cohen, T.J., Slack, M., Feathers, J.K., 2016. Sediment mixing in Aeolian sandsheets identified and quantified using single-grain optically stimulated luminescence. Quat. Geochronol. 32, 53–66. https://doi.org/10.1016/j.quageo.2015.12.006.
Green, A.N., Cooper, J.A.G., Loureiro, C., Dixon, S., Hahn, A., Zabel, M., 2022. Stormier mid-Holocene southwest Indian Ocean due to poleward trending tropical cyclones. Nat. Geosci. 15, 60–66. https://doi.org/10.1038/s41561-021-00842-w.
Grenfell, S.E., Ellery, W.N., Grenfell, M.C., 2009. Geomorphology and dynamics of the Mfolozi River floodplain, KwaZulu-Natal, South Africa. Geomorphology 107, 226–240. https://doi.org/10.1016/j.geomorph.2008.12.011.
Grenfell, S.E., Ellery, W.N., Grenfell, M.C., Ramsay, L.F., Flugel, T.J., 2010. Sedimentary facies and geomorphic evolution of a blocked-valley lake: Lake Futululu, northern Kwazulu-Natal, South Africa. Sedimentology 57 (5), 1159–1174. https://doi.org/10.1111/j.1365-3091.2009.01141.x.
Hagemans, K., Nooren, K., de Haas, T., Córdova, M., Hennekam, R., Stekelenburg, M.C. A., Rodbell, D.T., Middelkoop, H., Donders, T.H., 2021. Patterns of alluvial deposition in Andean lake consistent with ENSO trigger. Quat. Sci. Rev. 259, 106900. https://doi.org/10.1016/j.quascirev.2021.106900.
Hart, N.C.G., Washington, R., Reason, C.J.C., 2018. On the likelihood of tropical-extratropical cloud bands in the South Indian Convergence Zone during ENSO events. J. Clim. 31, 2797–2817. https://doi.org/10.1175/JCLI-D-17-0221.1.

Hogg, A.G., Heaton, T.J., Hua, Q., et al., 2020. SHCal20 Southern Hemisphere Calibration, 0–55,000 years cal BP. Radiocarbon 62 (4), 759–778. https://doi.org/10.1017/RDC.2020.59.

Humphries, M., Prior, K., Green, A., Vaughn, D., 2024. A 6000-year high-resolution composite record of El Niño-related drought in subtropical southeast Africa. Quat. Sci. Rev. 344, 108992. https://doi.org/10.1016/j.quascirev.2024.108992.

Humphries, M., Green, A., Higgs, C., Strachan, K., Hahn, A., Pillay, L., Zabel, M., 2020. High-resolution geochemical records of extreme drought in southeastern Africa during the past 7000 years. Quat. Sci. Rev. 236, 106294. https://doi.org/10.1016/j.quascirev.2020.106294.

Humphries, M.S., Green, A.N., Finch, J.M., 2016. Evidence of El Niño driven desiccation cycles in a shallow estuarine lake: the evolution and fate of Africa's largest estuarine system, Lake St Lucia. Global Planet. Change 147, 97–105. https://doi.org/10.1016/j.gloplacha.2016.11.002.

Humphries, M.S., Kirsten, K.L., McCarthy, T.S., 2019. Rapid changes in the hydroclimate of southeast Africa during the mid- to late-Holocene. Quat. Sci. Rev. 212, 178–186. https://doi.org/10.1016/j.quascirev.2019.04.006.

Intergovernmental Panel on Climate Change (IPCC), 2022. *Climate change 2022: impacts, adaption and vulnerability.* Contribution of working group II to the sixth assessment report of the intergovernmental panel on climate change. https://doi.org/10.1017/9781009325844.

Jongman, B., Winsemius, H.C., Aerts, J.C.J.H., de Perez, E.C., van Aalst, M.K., Kron, W., Ward, P.J., 2015. Declining vulnerability to river floods and the global benefits of adaptation. Proc. Natl. Acad. Sci. 112 (18), 2271–2280. https://doi.org/10.1073/pnas.1414439112.

Kandawasvika, G.Q., Thabethe, N., Dzangare, J., Manangazira, P., 2021. Impacts of tropical cyclones Idai and Kenneth on public health in Southern Africa. In: Nhamo, G., Chikodzi, D. (Eds.), Cyclones in Southern Africa. Sustainable Development Goals Series. Springer, Cham. https://doi.org/10.1007/978-3-030-74303-1_5.

Kendon, E.J., Stratton, R.A., Tucker, S., Marsham, J.H., Berthou, S., Rowell, D.P., Senior, C., 2019. Enhanced future changes in wet and dry extremes over Africa at convection-permitting scale. Nat. Commun. 10. https://doi.org/10.1038/s41467-019-09776-9.

Kovacs, Z.P., Du Plessis, D.B., Bracher, P.R., Dunn, P., Mallory, G.C.L., 1985. Documentation of the 1984 Domoina Floods. Department of Water Affairs, Republic of South Africa.

Kreutzer, S., Burow, C., Dietze, M., Fuchs, M.C., Schmidt, C., Fischer, M., Friedrich, J., 2018. Luminescence: comprehensive luminescence dating data analysis. R package version 0.9.20. https://CRAN.R-project.org/package=Luminescence.

Kruger, A.C., 1999. The influence of the decadal-scale variability of summer rainfall on the impact of El Niño and La Niña events in South Africa. Int. J. Climatol. 19, 59–68. https://doi.org/10.1002/(SICI)1097-0088(199901)19:1<59::AID-JOC347>3.0.CO;2-B.

Kruger, A.C., 2006. Observed trends in daily precipitation indices in South Africa: 1910-2004. Int. J. Climatol. 26, 2275–2285. https://doi.org/10.1002/joc.1368.

Lange, S., Volkholz, J., Geiger, T., Zhao, F., Vega, I., Veldkamp, T., Reyer, C.P.O., Warszawski, L., Huber, V., Jägermeyr, J., Schewe, J., Bresch, D.N., Büchner, M., Chang, J., Ciais, P., Dury, M., Emanuel, K., Folberth, C., Gerten, D., Gosling, S.N., Grillakis, M., Hanasaki, N., Henrot, A., Hickler, T., Honda, Y., Ito, A., Khabarov, N., Koutroulis, A., Liu, W., Müller, C., Nishina, K., Ostberg, S., Schmied, H.M., Seneviratne, S.I., Stacke, T., Steinkamp, J., Thiery, W., Wada, Y., Willner, S., Yang, H., Yoshikawa, M., Yue, C., Katja, Frieler, 2020. Projecting exposure to extreme climate impact events across six event categories and three spatial scales. Earths Future 8 (12). https://doi.org/10.1029/2020EF001616.

Lazenby, M.J., Todd, M.C., Wang, Y., 2016. Climate model simulation of the South Indian Ocean Convergence Zone: mean state and variability. Clim. Res. 68, 59–71. https://doi.org/10.3354/cr01382.

Lindsay, P., Mason, T.R., Pillay, S., Wright, C.I., 1996. Suspended particulate matter and dynamics of the Mfolozi estuary, KwaZulu-Natal: implications for environmental management. Environ. Geol. 28 (1), 40–51. https://doi.org/10.1007/s002540050077.

Liritzis, I., Stamoulis, K., Papachristodoulou, C., Ioannides, K., 2013. A re-evaluation of radiation dose-rate conversion factors. Mediterranean Archaeol. Archaeometr. 13 (3), 1–15.

Liu, W., Yang, T., Sun, F., Wang, H., Feng, Y., Du, M., 2021. Observation-constrained projection of global flood magnitudes with anthropogenic warming. Water Resour. Res. 57. https://doi.org/10.1029/2020WR028830.

Madsen, A.T., Duller, G.A.T., Donnelly, J.P., Roberts, H.M., Wintle, A.G., 2009. A chronology of hurricane landfalls at Little Sippewissett Marsh, Massachusetts, USA, using optical dating. Geomorphology 109 (1–2), 36–45. https://doi.org/10.1016/j.geomorph.2008.08.023.

Manhique, A.J., Reason, C.J.C., Rydberg, L., Fauchereau, N., 2011. ENSO and Indian Ocean sea surface temperatures and their relationships with tropical temperate troughs over Mozambique and the southwest Indian Ocean. Int. J. Climatol. 31, 1–13. https://doi.org/10.1002/joc.2050.

Mark, S.Z., Abbott, M.B., Rodbell, D.T., Moy, C.M., 2022. XRF analysis of Laguna Pallcacocha sediments yields new insights into Holocene El Niño development. Earth Planet Sci. Lett. 593, 117657. https://doi.org/10.1016/j.epsl.2022.117657.

Mayya, Y.S., Morthekai, P., Murari, M.K., Singhvi, A.K., 2006. Towards quantifying beta microdosimetric effects in single-grain quartz dose distribution. Radiat. Meas. 41 (7–8), 1032–1039. https://doi.org/10.1016/j.radmeas.2006.08.004.

McBride, C.M., Kruger, A.C., Dyson, L., 2022. Changes in extreme daily rainfall characteristics in South Africa: 1921–2020. Weather Clim. Extrem. 28, 100517. https://doi.org/10.1016/j.wace.2022.100517.

McCloskey, T.A., Liu, K., 2012. A 7000 year record of paleohurricane activity from a coastal wetland in Belize. Holocene 23 (2), 278–291. https://doi.org/10.1177/0959683612460782.

McGlue, M.M., Silva, A., Zani, H., Corradini, F.A., 2012. Lacustrine records of Holocene flood pulse dynamics in the Upper Paraguay River watershed (pantanal wetlands, Brazil). Quat. Res. 78 (2), 285–294. https://doi.org/10.1016/j.yqres.2012.05.015.

Mejdahl, V., 1979. Thermoluminescence dating: Beta-dose attenuation in quartz grains. Archaeometry 21 (1), 61–72. https://doi.org/10.1111/j.1475-4754.1979.tb00241.x.

Miller, C., Finch, J., Hill, T., Peterse, F., Humphries, M., Zabel, M., Schefuß, E., 2019. Late Quaternary climate variability at Mfabeni peatland, eastern South Africa. Clim. Past 15 (3), 1153–1170. https://doi.org/10.5194/cp-15-1153-2019.

Moy, C.M., Seltzer, G.O., Rodbell, D.T., Anderson, D.M., 2002. Variability of El Niño/Southern Oscillation activity at millennial timescales during the Holocene epoch. Nature 420, 162–165. https://doi.org/10.1038/nature01194.

Murray, A.S., Aitken, M.J., 1988. Analysis of low-level natural radioactivity in small mineral samples for use in thermoluminescence dating, using high-resolution gamma spectrometry. International Journal of Radiation Applications and Instrumentation. Part A. Appl. Radiat. Isot. 39, 145–158.

Murray, A.S., Olley, J.M., 2002. Precision and accuracy in the optically stimulated luminescence dating of sedimentary quartz: a status review. Geochronometria 21, 1–16.

Murray, A.S., Wintle, A.G., 2000. Luminescence dating of quartz using an improved single-aliquot regenerative-dose protocol. Radiat. Meas. 32, 57–73. https://doi.org/10.1016/S1350-4487(99)00253-X.

Murray, A.S., Wintle, A.G., 2003. The single aliquot regenerative dose protocol: potential for improvements in reliability. Radiat. Meas. 37, 377–381. https://doi.org/10.1016/S1350-4487(03)00053-2.

NASA/METI/AIST/Japan Spacesystems and U.S./Japan ASTER Science Team, 2019. *ASTER global digital elevation model V003* [ASTGTMV003_S29E032_dem]. NASA EOSDIS Land Process. DAAC. https://doi.org/10.5067/ASTER/ASTGTM.003, 2021-02-11.

Nelson, M.S., Rittenour, T.M., 2015. Using grain-size characteristics to model soil water content: application to dose-rate calculation for luminescence dating. Radiat. Meas. 81, 142–149. https://doi.org/10.1016/j.radmeas.2015.02.016.

Neumann, F.H., Scott, L., Bousman, C.B., van As, L., 2010. A Holocene sequence of vegetation change at Lake Eteza, coastal KwaZulu-Natal, South Africa. Rev. Palaeobot. Palynol. 162, 39–53. https://doi.org/10.1016/j.revpalbo.2010.05.001.

Nhundu, K., Sibanda, M., Chaminuka, P., 2021. Economic losses from cyclones Idai and Kenneth and floods in Southern Africa: implications on sustainable development goals. In: Nhamo, G., Chikodzi, D. (Eds.), Cyclones in Southern Africa. Sustainable Development Goals Series. Springer, Cham. https://doi.org/10.1007/978-3-030-74303-1_19.

Olley, J.M., Murray, A.S., Roberts, R.G., 1996. The effects of disequilibria in the uranium and thorium decay chains on burial dose rates in fluvial sediments. Quat. Sci. Rev. 15, 751–760. https://doi.org/10.1016/0277-3791(96)00026-1.

Peng, J., 2021. Analyzing statistical age models to determines the equivalent dose and burial age using a Markov Chain Monte Carlo method. Geochronometeria 48, 147–160. https://doi.org/10.1515/geochr-2015-0114.

Prescott, J.R., Hutton, J.T., 1994. 'Cosmic ray contributions to dose rates for luminescence and ESR dating: large depths and long-term time variations. Radiat. Meas. 23 (2/3), 497–500. https://doi.org/10.1016/1350-4487(94)90086-8.

Rapolaki, R.S., Blamey, R.C., Hermes, J.C., Reason, C.J.C., 2019. A classification of synoptic weather patterns linked to extreme rainfall over the Limpopo River Basin in southern Africa. Clim. Dyn. 53, 2265–2279. https://doi.org/10.1007/s00382-019-04829-7.

Reason, C.J.C., Mulenga, H., 1999. Relationships between South African rainfall and SST anomalies in the southwest Indian Ocean. Int. J. Climatol. 19, 1651–1673. https://doi.org/10.1002/(SICI)1097-0088(199912)19:15<1651::AID-JOC439>3.0.CO;2-U.

Rees-Jones, J., 1995. Optical dating of young sediments using fine-grain quartz. Ancient TL 13 (2), 9–14. https://doi.org/10.26034/la.atl.1995.242.

Rittenour, T.M., 2008. Luminescence dating of fluvial deposits: applications to geomorphic, palaeoseismic and archaeological research. Boreas 37, 613–635. https://doi.org/10.1111/j.1502-3885.2008.00056.x.

Rodnight, H., Duller, G.A.T., Wintle, A.G., Tooth, S., 2006. Assessing the reproducibility and accuracy of optical dating fluvial deposits. Quat. Geochronol. 1 (2), 109–120. https://doi.org/10.1016/j.quageo.2006.05.017.

Santisteban, J.I., Mediavilla, R., de Frutos, L.G., Cilla, I.L., 2019. Holocene floods in a complex fluvial wetland in central Spain: environmental variability, climate and time. Global Planet. Change 181, 1–16. https://doi.org/10.1016/j.gloplacha.2019.102986.

Stager, J.C., Ryves, D.B., King, C., Madson, J., Hazzard, M., Neumann, F.H., Maud, R., 2013. Late Holocene precipitation variability in the summer rainfall region of South Africa. Quat. Sci. Rev. 67, 105–120. https://doi.org/10.1016/j.quascirev.2013.01.022.

Tanoue, M., Hirabayashi, Y., Ikeuchi, H., 2016. Global-scale river flood vulnerability in the last 50 years. Sci. Rep. 6, 36021. https://doi.org/10.1038/srep36021.

The Centre for Research on the Epidemiology of Disasters (CRED) and The UN Office for Disaster Risk Reduction (UNDRR), 2020. Human cost of disasters: an overview of the last 20 years (2000-2019). https://cred.be/sites/default/files/CRED-Disaster-Report-Human-Cost2000-2019.pdf.

Thompson, J.A., Chen, J., Yang, H., Li, T., Bookhagen, B., Burbank, D., 2018. Coarse- versus fine-grain quartz OSL and cosmogenic ^{10}Be dating of deformed fluvial terraces on the northwest Pamir margin, northwest China. Quat. Geochronol. 46, 1–15. https://doi.org/10.1016/j.quageo.2018.01.002.

Thomsen, K.J., Murray, A., Jain, M., 2012. The dose dependency of the over-dispersion of quartz OSL single grain dose distributions. Radiat. Meas. 47 (9), 732–739. https://doi.org/10.1016/j.radmeas.2012.02.015.

Tim, N., Hünicke, B., Zorita, E., 2023. Simulated rainfall extremes over southern Africa over the 20th and 21st centuries. Nat. Hazards Earth Syst. Discuss. [preprint]. https://doi.org/10.5194/nhess-2023-147.

Umfolozi Sugar Mill, 2015. *Umfolozi sugar mill history*. South Africa. http://www.umfolozisugarmill.co.za/page.aspx?ID=5855. Accessed: 21st December 2015.

Wintle, A.G., Murray, A.S., 2006. A review of quartz optically stimulated luminescence characteristics and their relevance in single-aliquot regeneration dating protocols. Radiat. Meas. 41 (4), 369–391. https://doi.org/10.1016/j.radmeas.2005.11.001.

Wood, J.C., 2015. Section 1.2.3: determination of moisture content and total organic carbon within basin environments: Loss-on-ignition. In: Cook, S.J., Clarke, L.E., Nield, J.M. (Eds.), Geomorphological Techniques (Online Edition). British Society for Geomorphology, London, pp. 1–7.

Wood, J.C., 2020. Palaeoflood Chronology of blocked-valley Lakes in Eastern South Africa. University of Gloucestershire. https://doi.org/10.46289/9JL99YR8. PhD thesis.

Zhang, W., Zhou, T., Zou, L., Zhang, L., Chen, X., 2018. Reduced exposure to extreme precipitation from 0.5 °C less warming in global land monsoon regions. Nat. Commun. 9. https://doi.org/10.1038/s41467-018-05633-3.

Zimmerman, D.W., 1971. Thermoluminescent dating using fine grains from pottery. Archaeometry 13 (1), 29–52. https://doi.org/10.1111/j.1475-4754.1971.tb00028.x.